Multi-physics modelling of the pellet-to-cladding gap closure phenomenon for SFR fuel performance codes

Mourad Temmar, Bruno Michel, Isabelle Ramière, Nicolas Favrie

Multi-physics modelling of the pellet-to-cladding gap closure phenomenon for SFR fuel performance codes

M. Temmar, B. Michel, I. Ramiere, N. Favrie

PII: S0022-3115(19)30899-2

DOI: https://doi.org/10.1016/j.jnucmat.2019.151909

Reference: NUMA 151909

To appear in: *Journal of Nuclear Materials*

Received Date: 9 July 2019

Revised Date: 21 October 2019

Accepted Date: 13 November 2019

Please cite this article as: M. Temmar, B. Michel, I. Ramiere, N. Favrie, Multi-physics modelling of the pellet-to-cladding gap closure phenomenon for SFR fuel performance codes, *Journal of Nuclear Materials* (2019), doi: https://doi.org/10.1016/j.jnucmat.2019.151909.

Multi-physics modelling of the pellet-to-cladding gap closure phenomenon for SFR fuel performance codes

M. Temmar*, B. Michel*, I. Ramiere*, N. Favrie**

* CEA, DEN, DEC, SESC, LSC bat 151 Centre de Cadarache 13108 Saint Paul Lez Durance France

** Aix-Marseille Université, C.N.R.S. U.M.R. 7343, IUSTI, 5 rue E. Fermi, 13453 Marseille Cedex 13, France

ABSTRACT

The reference fuel design for french Sodium nuclear Fast Reactor (SFR) consists of fuel pins made of $(U,Pu)O_2$ pellets inserted in a steel alloy cladding tube. Fuel pin behaviour under irradiation is complex and simulated with SFR fuel performance codes through the world. Concerning the thermal behaviour, the pellet-to-cladding gap evolution has a strong impact on the fuel maximal temperature and hence has to be precisely modelled. Based on experimental observations, the gap size evolution seems to be related to two phenomena: one related to the effect of pellet fragmentation and the second one related to a porosity migration phenomenon. The second phenomenon is due to the presence of high thermal radial gradients and leads to a fuel restructuration. The aims of this work are first to investigate with 3D simulation the impact of the fuel restructuration and of the fuel fragmentation on the pellet fragments radial displacement, and then to propose a new 1D physically based relocation model and its coupling formulation with the SFR codes multi-physics computational scheme. Thanks to these new developments the pellet-to-cladding gap closure simulation and hence the pellet temperature assessment, can be improved in a 1D fuel performance code.

This work has been done in the framework of a cooperative program between CEA, FRAMATOME and EDF, devoted to the development of the fuel elements for GENIV Reactors.

1. INTRODUCTION

In french Sodium nuclear Fast Reactor (SFR), fuel pins are made of fuel pellets (cylinder of approximately one centimeter height and diameter) inserted in a steel cladding (annular cylinder of few meters height and half millimeter thickness). A gap of around 100 micrometers, called pellet-to-cladding gap in the sequel, initially filled with helium separates them. During irradiation the fuel pins are submitted to hard environments, leading to high temperatures and high temperature gradients, inducing various phenomena: namely, fuel fragmentation, fuel pellet restructuring characterized by the central hole formation, fission gas release, geometrical and property change of the pellet-to-cladding gap. These phenomena are represented with some various assumptions by numerical models implemented in so called “1.5D” fuel performance codes in order to understand and predict the behaviour of SFR fuel pins. One can for example cite GERMINAL (France [1]), BERKUT (Russia [2], [3] and [4]), CEPTAR (Japan [5]), FEAST-OXIDE (US [6] and [7]), TRAFIC (UK [8]), FIBER-OXIDE (China [9]) and others codes ([10] and [11]). Full 3D codes, modelling the complex behaviour of SFR fuel pins, can be expected in few years thanks to High Performance Computing. Nevertheless, “1.5D” codes, needed for their short computation times, enable us to simulate the main phenomena appearing in a whole fuel pin, and therefore to obtain a satisfactory representation of the fuel behaviour during irradiation.

These “1.5D” codes focus on a single fuel pin. The fuel pin is represented by a stack of slices, each of them being modelled by a 1D axisymmetric hypothesis. This “1.5D” representation allows to determine the local behaviour of the fuel and its surrounding cladding by taking into account linear power and coolant temperature variations along the fuel element. But this simple geometrical representation cannot always provide a detailed description of some complex phenomena, where multi-dimensional aspects are involved. To obtain a better fuel behaviour prediction, these fuel performance codes are still improving the physics of their models. Among these improvements, one concerns the fuel temperature evolution during irradiation

regarding the fuel melting safety margin. Indeed, all phenomena taking place in a fuel pin are controlled by the temperature, and consequently a good precision of the temperature is of principal importance in modelling the fuel pin behaviour.

The fuel thermal power evacuation depends greatly on the heat transfer coefficient in the pellet-to-cladding gap. This coefficient can be defined as the ratio of the average thermal conductivity coefficient of the gas mixture over the gap thickness. Hence, the gap size influences considerably the heat exchange between the fuel and the cladding, and by consequence the fuel temperature evolution. During irradiation, the gap, initially filled of helium, is polluted by fission gas released leading to a decrease of the average thermal conductivity in the gap. This degradation of the gas mixture thermal conductivity is compensated by the gap size reduction, which allows to finally decrease the fuel temperature.

The aim of this paper is to refine our understanding of the phenomena responsible of the gap size reduction in order to improve the current related models implemented in 1.5D SFR fuel performance codes. This better modelling may lead to a reduction of the uncertainty on the maximum fuel temperature assessment and the fuel melting margin.

For this purpose a two-step process has been pursued. First, a 3D thermo-mechanical modelling representing one pellet with the associated piece of cladding has been proposed in the LICOS [12] prototype code of the PLEIADES platform [14]. This 3D simulation allow us to identify the main mechanisms responsible for gap size reduction and to assess their impact on the fuel temperature evolution during irradiation. Based on the obtained 3D results, the second step consists in proposing a 1D gap size reduction formulation modelling the identified mechanisms. This model is finally implementing in the GERMINAL [1] computational scheme. Simulation results in 3D and 1D are presented for various fuel pins and compared with experimental results in order to assess the validity and the improvement brought by this new formulation.

2. WORKS STATEMENT ON SFR FUEL-TO-CLADDING GAP CLOSURE MECHANISM

Some fuel performance codes yet incorporate models that aim to simulate the reduction of pellet-to-cladding gap size and its impact on the thermal evolution of the fuel. This is the case, for example, in GERMINAL [1], FEAST OXIDE ([6] and [7]) and FIBRE OXIDE [9] codes. Each of these codes has a specific model called « relocation model» allowing to represent in 1D the movement of the fuel in the radial direction and its impact on the thermal transfer between the pellet and the cladding. These relocation models try to reproduce the main phenomena responsible for gap size evolution which can't be explicitly represented with a 1D geometry. For example a well-known phenomenon simulated by a relocation model is the fuel pellet fragmentation and its associated hourglass effect induced by the thermal gradient.

The GERMINAL relocation model is based on a fictive homogeneous inelastic strain which is taken into account in the mechanical behaviour law, while FIBRE OXIDE and FEAST OXIDE use a displacement formulation. All these models are based on empiric equations which depend on several parameters (e.g linear power, geometry, temperature, gap thickness) and are fitted on experimental measures. Adjustments realized on the parameters of these relocation models allow to obtain a good agreement between numerical and experimental results, but some phenomena responsible of the pellet-to-cladding gap closure are not properly identified and therefore the obtained models are non-predictive. Others codes that do not have a specific relocation model, use different kind of strategy to model the effect of the reduction of the gap thickness. For example, the CEPTAR code, directly modifies the heat exchange coefficient of the pellet-to-cladding gap to obtain a good fuel temperature estimation ([5]). On the other hand, the BERKUT code considers that the solid and the gaseous swellings due to irradiation are the only phenomena explaining the gap closure ([2], [3] and [4]).

3. GAP CLOSURE PHENOMENA AND MODELLING HYPOTHESES

Based on experimental results ([15], [16] and [17]), we have identified two gap reduction phenomena occurring at the beginning of irradiation and leading to the gap closure. The first one, already well known, is related to the pellet fragmentation (Figure 1 a). The second one that we proposed is related to the mass transfer associated to the fuel restructuration (Figure 1 b).

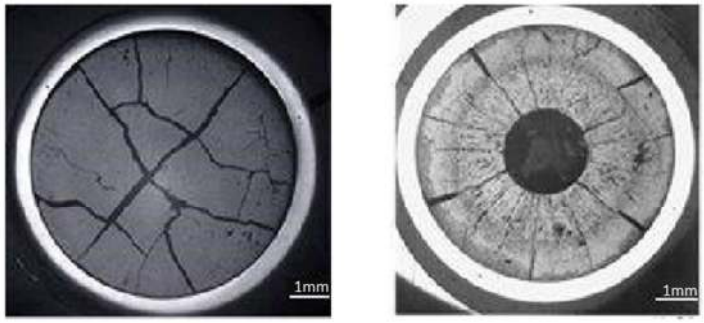

a) Fuel fragmentation b) Fuel restructuration [18]

Figure 1 – Phenomena responsible of the pellet-to-cladding gap reduction

3.1. Fuel fragmentation

Pellet fragmentation under LWR irradiation conditions and its consequences on the fuel pellet fragment relocation and gap closure have been studied in references [20], [21], [22] and [23]. A mechanical model of a single pellet fragment is proposed in reference [24] in order to assess stress and strain fields in a 1D PWR fuel performance code. However, relocation models proposed by all these authors remain empirical with a fit of parameters derived from the integral experimental results. The objective of this new work is to derive the constitutive equations of the relocation model from the mechanical analysis of the fragmented pellet. Thanks to this approach the analytical expression of the relocation strain, given in section 5.2.1, can be justified with each physical aspect involved in the pellet to cladding gap closure induced by pellet fragmentation.

Fuel fragmentation is the first phenomenon that appears during irradiation due to a high radial thermal gradient reaching several thousands of kelvins per centimetre as mentioned in reference [19]. More precisely, the pellet cladding differential thermal expansion leads to a first reduction of the pellet-to-cladding gap size (cf step 0-1 in Figure 2). Then, the thermomechanical stresses, induced by the thermal gradient, exceeds the fuel rupture strength. The pellet fragmentation implies that the elastic strains under the thermal gradient generate a curvature of the inter-fragment surfaces as shown in Figure 2 step 2. This curvature and the contact condition between pellet fragments explain a significant increase of the radial relocation displacement in comparison with an un-fragmented pellet (ΔU_r on the Figure 2 below). Moreover, the thermal gradient leads to the well-known “hourglass” shape (see for example [25] and [26]) of the pellet as illustrated in Figure 3 (a). The axial curvature of the pellet fragment increases significantly the radial relocation displacement at inter-pellet plane allowing to first close the pellet-to-cladding gap at this plane. Hence the pellet-to-cladding gap size also depends on the axial position between the mid and the inter pellet planes as illustrated in Figure 3 (b).

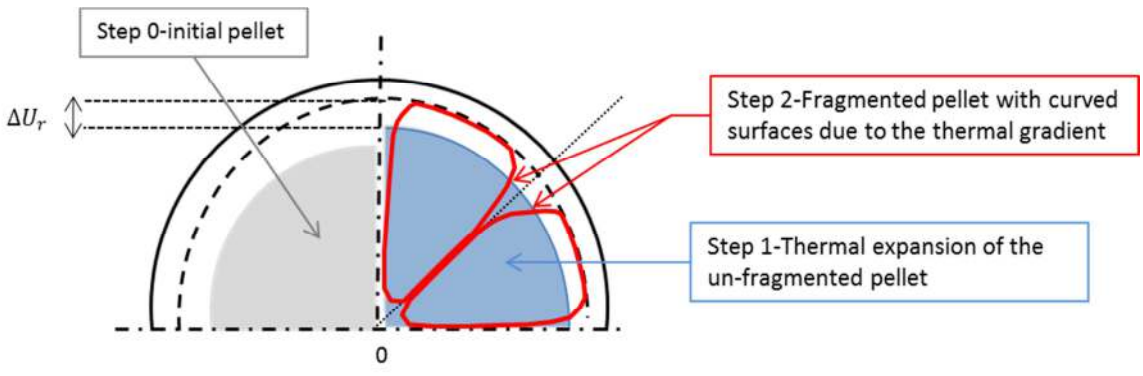

Figure 2 – Impact of thermal gradient on fragmented and un-fragmented pellet

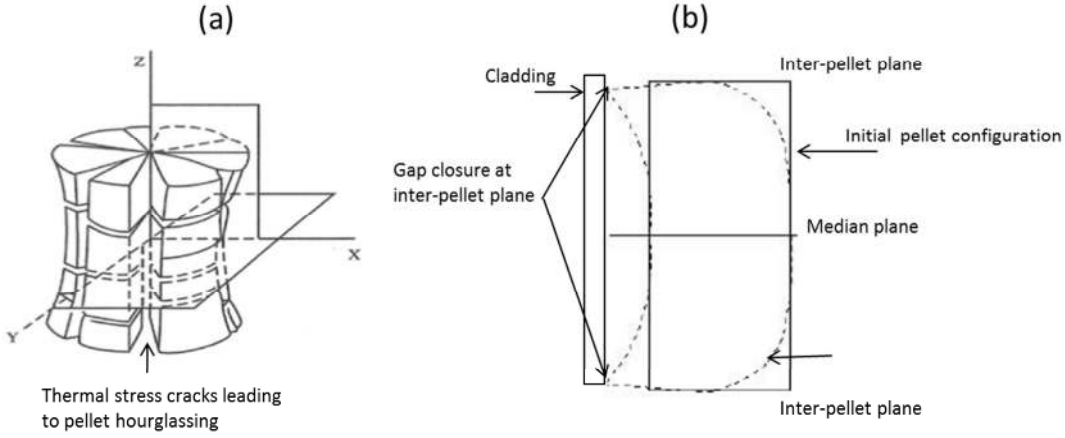

Figure 3 – Representation of the hourglass shape [25] and [26]

3.2. Fuel restructuration

The fuel restructuration and the associated central hole formation are also due to high temperatures and high radial thermal gradients occuring in SFR fuel pins. These modifications of the material are induced by pores migration toward the fuel center (higher temperature). This migration is due to an evaporation-condensation mechanism, where oxydes molecules evaporate from the hottest free surface of a pore or a microcrack, then diffuse through the gaseous phase and finally condense on the coolest free surface. This migration process is activated when the temperature exceeds 1800 °C [15]. During their migration toward the center, pores sweep grains which induces a fuel restructuration with a columnar grains microstructure [15]. This restructuration mechanism has been proposed according the ceramographic observations where we can see some small voids found in the trace of the edge of the lenticular void according a migration direction toward the pellet center (see Figure 4 from reference [16]). Then, due to this oriented migration process it has been deduced that pores gathering in the pellet center lead to the central hole formation as illustrated in Figure 4. In reference [16] porosity migration is mainly attributed to lenticular voids which were supposed to be initialy disc-shaped pores due to the fabrication process. This geometrical modification from a disc-shape to a lenticular shape has been explained in [16] through a 2D simulation of the vapour phase transport.

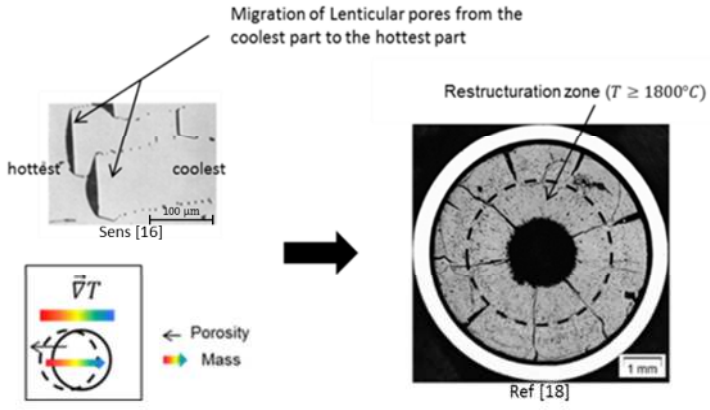

Figure 4 – Evaporation-condensation phenomenon

Concerning the migration of free volumes induced by cracks, the comprehension of the evaporation-condensation mechanism is still a difficult issue. As illustrated in Figure 5, the fuel restructuration allows to partially heal cracks initiated at the first power increase. To explain crack healing, Bain [27] has suggested the grain growth occurring after irradiation. Other authors [28], [29] suggest that the healing process is controlled by a mass transport phenomenon (diffusion or evaporation-condensation) independently from the grain growth. According to Hoffmann [17], the main mass transport phenomenon

involved in crack healing under SFR irradiation condition is evaporation-condensation. To explain the healing process induced by the evaporation-condensation mass transport, Sens and Hoffmann [16] [17] suggested that cracks act like a source of lenticular voids, near the free surface, which then migrate in the bulk by evaporation-condensation under the thermal gradient. This explanation was based on experimental observations where a lot small lenticular voids were observed near the crack surfaces (see Figure 3 in [16] and Figure 1 in [17]). If we refer to these experimental results it seems that manufacturing pores and crack free volumes both lead to mass transport through an evaporation-condensation mechanism, however the associated pores velocity can be different. Indeed in the case of cracks we need to add the time needed for the void nucleation in the bulk. In this work, we will assume that this nucleation time is negligible, which means that the pores velocity will be the same for both cases (see advection equation (10) in section 4.5.1).

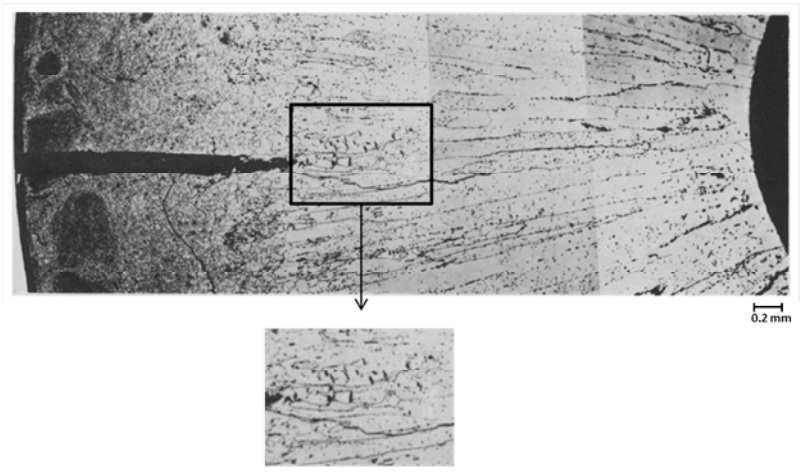

Figure 5 – Crack healing by production and migration of lenticular pore [17]

Micrographic analyses (see for example Figure 5) suggest that the mass transfer and associated crack healing in the restructuring zone increases this zone volume and consequently the circumferential opening of the cracks in the periphery. These last point can explain an increase of the pellet diameter in comparison with an un-restructured pellet and then to a closure of the pellet-to-cladding gap.

Based on this observation, we have proposed a coupling mechanism between mass transfer and fragments radial relocation to properly simulate the gap size reduction (see Figure 8). In this mechanism, we consider that the fuel dense volume leaving the pellet center by evaporation-condensation is decomposed into two parts: one part fills the manufacturing pores and the other one being layered between the pellet fragments (see red parallelepiped in Figure 8), both in the columnar grains zone where the fuel has been restructured. According to this proposal, the volume change of the restructuring zone will lead to the radial fragment relocation (Figure 8). In this approach the mass conservation principle is considered independently from the mechanical displacement field, which means that the relocation displacement contribution refers to an initial configuration.

4. 3D SIMULATION OF GAP CLOSURE PHENOMENA

4.1. 3D simulation

In order to evaluate if the two previous identified mechanisms (fuel fragmentation and mass transfer) enable to describe the pellet-to-cladding gap size evolution, a 3D model has been proposed. The pellet fragmentation is described thanks to a 3D finite element mesh of a single fragment and appropriate boundary conditions as proposed for pellet cladding mechanical interaction simulation [13]. On the other hand, an extension of this 3D approach has been proposed (see section 4.5) in order to model the fuel restructuration relocation mechanism presented in Figure 8. This multi-physics 3D simulation has been realized thanks to a one-way coupling process between the 1.5D code GERMINAL and the 3D prototype application LICOS, both in the PLEIADES numerical platform [14].

4.2. Geometry and boundary conditions

Based on the PCI modelling assumption [13], the modelled fragment represents 1/8 of the fuel pellet and its associated piece of cladding in order to maximize the pellet hourglass shape magnitude. Axial and circumferential symmetrical considerations allow us to study only one quarter of this pellet fragment. Looking at Figure 6, symmetry boundary conditions are hence applied on the surface $S5_c, S3_c, S4_c$ and $S4_p$. The mechanical interaction with the rest of the fuel pin is modelled thanks to the following boundary conditions:

- At the inter-pellet plane $S5_p$: $U_z \geq 0$ (allowing to simulate the "hourglass" shape),
- At the inter-fragment plane $S3_p : U_\theta \geq 0$ (allowing to simulate the effect of the pellet fragmentation as illustrated in Figure 2),
- Between the pellet and cladding when the contact is established on $S6_p$ and $S1_c$: contact with friction,
- Pellet median plane and cladding median plane are submitted to a kinematic relation congruent with the generalized plane strain hypothesis ($U_z = Up$ on $S2_p$ and $Uz = Uc$ on $S2_c$), with a locking condition of the two planes when the pellet-to-cladding gap is closed ($Up - Uc = constant$).

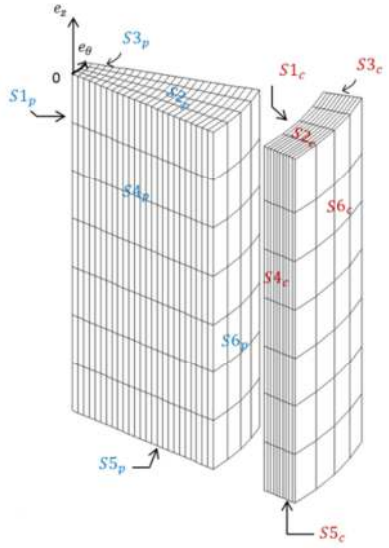

Figure 6 – 3D representation of a SFR fragment of pellet and its associated piece of cladding

4.3. Physicochemical and thermomechanical coupling scheme

To take into account the physicochemical state in our 3D model, we used a one-way coupling scheme between GERMINAL and LICOS. This method allows us to use as input of the 3D scheme, some physical variables pre-computed by GERMINAL. Only the physical variables required for the thermomechanical computation are concerned by this coupling. We hence have selected the following coupling variables:

- gas content and pressure in the pellet-to-cladding gap
- Sodium coolant temperature
- mean power density and burnup in the pellet
- mean pellet porosity
- fuel densification and swelling under irradiation
- columnar grain radius
- central hole radius

All these input data are time and sometimes space dependent. Concerning the latter case, the 3D input field is built from the 1D GERMINAL output field thanks to a kriging technique based on an axisymmetric cylindrical geometrical assumption [30]. The 3D thermomechanical LICOS computational scheme solved at each time-step is represented on Figure 7 where pre-computed data coming from GERMINAL are prescribed as external irradiation loadings. An internal thermomechanical convergence loop is performed. In case of thermomechanical resolution divergence, an adaptive time-step algorithm is then used.

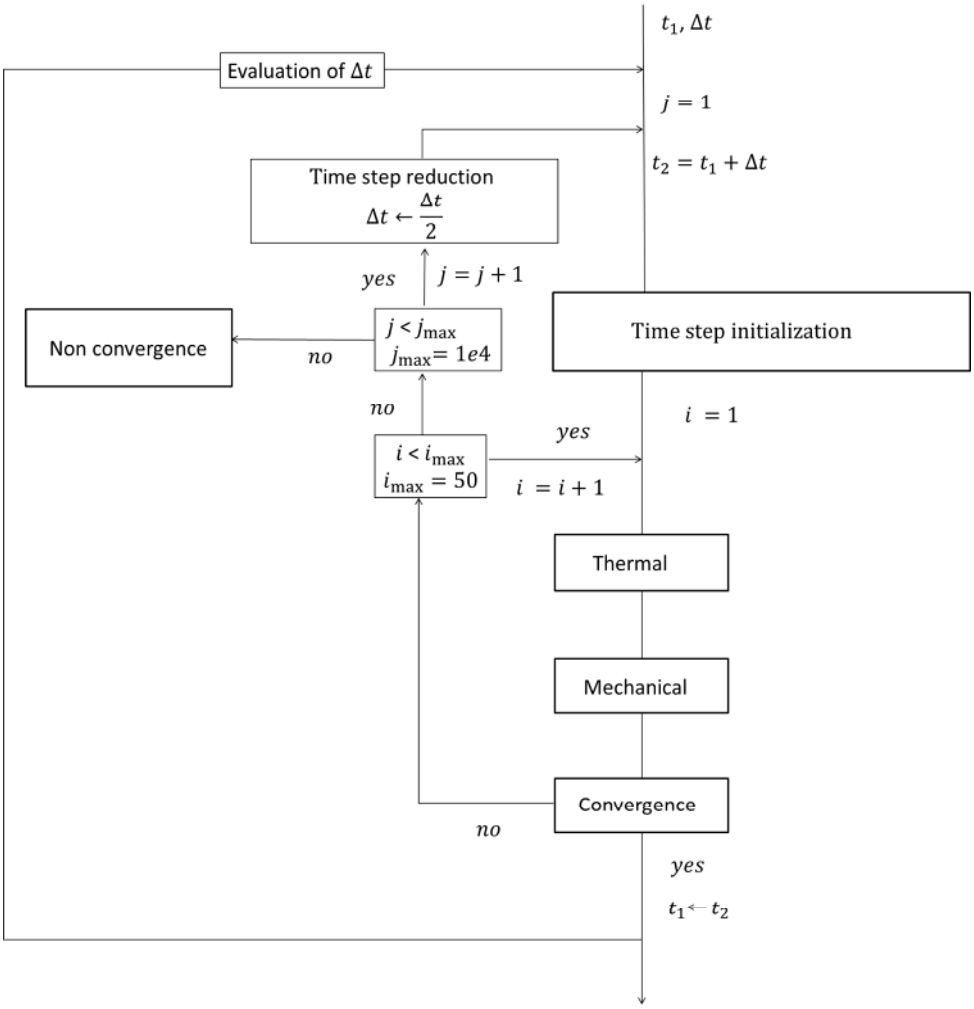

Figure 7 – LICOS thermo-mechanical computational scheme

The following sections are devoted to the description of each model of the 3D computational scheme.

4.4. Thermomechanical models

The 3D scheme uses the same mechanical and thermal models than GERMINAL ([1] and [31]).

4.4.1. Thermal model

The thermal model allows us to determine the variation of the temperature field by solving the heat equation in the pellet and the cladding:

$$\rho c_p \frac{\partial T}{\partial t} = \mathrm{div}\left(\lambda \overrightarrow{\mathrm{grad}T}\right) + p_v \qquad (1)$$

With T the temperature, ρ the density, c_p the heat capacity, λ the thermal conductivity and p_v the mean power density in the fuel.

The thermal flow through the gas present in the pellet-to-cladding gap is calculated as follows:

$$\Phi = \mathrm{h}\left(T, e_{gap}, \chi_{g_i}, R_a\right)(\mathrm{T_{clad}} - \mathrm{T_{pellet}}) \quad (2)$$

with $\mathrm{h}\left(T, e_{gap}, \chi_{g_i}, R_a\right)$ the nonlinear heat transfer coefficient homogenized which depends on the temperature T, the gap size e_{gap}, the gas composition χ_{g_i} and the contact roughness R_a in case of a closed gap (see reference [1] for more details on the mathematical expression of h), $\mathrm{T_{clad}}$ is the internal surface temperature on the cladding and $\mathrm{T_{pellet}}$ the external surface temperature on the pellet. In the computation scheme of section 4.3 the thermo-mechanical coupling, induced by the heat transfer through the gap, is assessed with the local radial gap size, which depends on the circumferential and axial positions and is a result of the 3D mechanical computation.

The studied pellet fragment and the associated cladding are submitted to thermal loadings which are derived from the one way coupling method explained previously, namely:

- Mean power density induced by fission reaction applied as a power source in the pellet "$\mathrm{p_v}$".
- Sodium coolant temperature applied as Dirichlet boundary condition on the cladding external radius $\mathrm{S6_c}$ (see Figure 6).

4.4.2. Mechanical model

The displacement field is calculated through the resolution of the nonlinear static equilibrium (equation (3)) thanks a weak formulation with the finite element method. The double bar on top of a symbole denote a second order tensor.

$$\begin{cases} \mathrm{div}\overline{\overline{\sigma}} = 0 \text{ in } \Omega \\ \overline{\overline{\sigma}}\,\vec{n} = \vec{\Sigma}_{\mathrm{imp}} \text{ on } \partial\Omega_{\mathrm{T}} \\ \vec{u}^{\mathrm{mec}} = \vec{U}_{\mathrm{imp}} \text{ on } \partial\Omega_{\mathrm{u}} \end{cases} \quad \text{such as, } \partial\Omega_{\mathrm{T}} \cap \partial\Omega_{\mathrm{u}} = \emptyset \text{ and } \partial\Omega_{\mathrm{T}} \cup \partial\Omega_{\mathrm{u}} = \partial\Omega \quad (3)$$

We consider a domain Ω of boundary $\partial\Omega$. This boundary is partitioned into two disjointed parts $\partial\Omega_{\mathrm{T}}$ and partial $\partial\Omega$u on which imposed displacement $\vec{U}_{\mathrm{imp}}$ and imposed forces $\vec{\Sigma}_{\mathrm{imp}}$ are respectively applied.

The material behaviour is given by the following constitutive law:

$$\dot{\overline{\overline{\sigma}}} = \underline{\underline{\underline{\underline{E}}}} : (\dot{\overline{\overline{\varepsilon}}}^{\mathrm{tot}} - \dot{\overline{\overline{\varepsilon}}}^{\mathrm{th}} - \dot{\overline{\overline{\varepsilon}}}^{\mathrm{plast}} - \dot{\overline{\overline{\varepsilon}}}^{\mathrm{creep}} - \dot{\overline{\overline{\varepsilon}}}^{\mathrm{swell}}) \quad (4)$$

The mechanical model allows to take into account the material stiffness cancelation due to the central hole resulting of the pores migration toward the pellet center (equation (5))

$$\overline{\overline{\sigma}} = 0 \quad (5)$$

where $\underline{\underline{\underline{\underline{E}}}}$ is the Hooke fourth order tensor, $\dot{\overline{\overline{\varepsilon}}}^{\mathrm{tot}}$ is the total strain rate according to the small strain assumption, $\dot{\overline{\overline{\varepsilon}}}^{\mathrm{th}}$ is the thermal expansion strain rate, $\dot{\overline{\overline{\varepsilon}}}^{\mathrm{plast}}$ is the plastic strain rate, $\dot{\overline{\overline{\varepsilon}}}^{\mathrm{creep}}$ is the thermal and irradiation creep strain rate and $\dot{\overline{\overline{\varepsilon}}}^{\mathrm{swell}}$ is the strain rate induced by the isotropic irradiation swelling. Strain rate expressions are proper to each material (fuel or cladding).

Mechanical loading boundary conditions are defined as follows:

- Pressure imposed on $\mathrm{S1_p}$, $\mathrm{S6_p}$, $\mathrm{S3_p}$ and $\mathrm{S1_c}$ due to fission gas release (see Figure 6 for surface names).
- Axial resultant (on $\mathrm{S2_p}$ and $\mathrm{S2_c}$) due to end effect of the internal pressure imposed on the cladding and pellet median planes.

4.5. Time step initialization : fuel relocation by mass transfer

4.5.1. Mass transfer geometrical representation

The 3D mechanical formulation presented in previous sections doesn't allow us to simulate directly the mass transfer mechanism proposed in section 3.2 (see Figure 8). The fuel relocation induced by the mass transfer is then simulated by a fuel

volume expansion of the restructured zone. According the assumption that this volume expansion doesn't affect the pellet fragment internal mechanical equilibrium, the associated geometric transformation is performed outside of the mechanical computation, in the time step initialization model (see Figure 7). The geometrical transformation is calculated at each time step as a function of the dense volume to be inserted between fragments. This volume is assumed to have a parallelepiped shape.

Considering the mass transfer mechanism proposed in section 3.2, the fuel dense volume $V_{mass\ transfer}$ which migrates in the restructuring zone (see Figure 8), can be decomposed as the sum of a volume $V^{man}_{mass\ transfer}$ that migrates into the manufacturing pores and another volume $V^{fill}_{mass\ transfer}$ filling the zone between pellet fragments (see Figure 8):

$$V_{mass\ transfer}(t) = V^{man}_{mass\ transfer}(t) + V^{fill}_{mass\ transfer}(t) \quad (6)$$

According the mass balance equation, the total dense volume transferred $V_{mass\ transfer}$ is given by the central hole volume V_{hole}, computed for the initial geometry, and the initial manufacturing porosity p^{man}_{ini} as follows:

$$V_{mass\ transfer}(t) = V_{hole}(t)(1 - p^{man}_{ini}) \quad (7)$$

The potential volume available for the mass transfer between the pellet fragments V^{fill} can be defined from the fuel pin geometry at the first order as the free volume in the pellet-to-cladding gap when the restructuring process begins (i.e when the maximal temperature exceed 1800 °C). Indeed, before the pores begin to migrate, the gap size is mainly reduced due to the thermal expansion of the fuel pellet. Hence, we take in consideration the pellet and cladding differential thermal expansion up to a temperature of 1800 °C to determine this potential volume fraction available for filling the zone between pellet fragments (Figure 8). This differential thermal expansion has been computed under the assumption of an isotropic elastic behaviour, a plane strain condition, axisymmetric condition and no external forces according the analytical solution given in the further section 5.2.1.2 for a full or an annular cylinder. For the numerical application we consider fuel central and external temperatures of 1850°C and 900°C respectively, and a constant temperature of 500°C in the cladding.

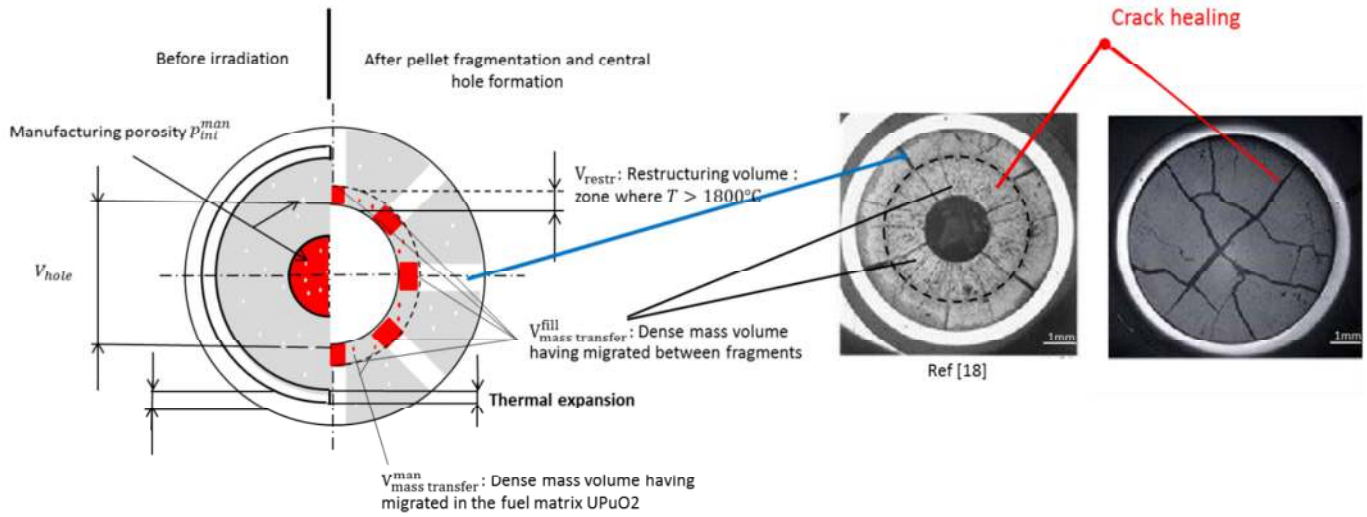

Figure 8 - The potential volume fraction available between pellet fragments

The initial filling porosity associated to the volume V^{fill} is defined with the volume fraction as following:

$$p^{fill}_{ini} = \frac{v^{fill}}{V_{pellet}(t_{restructuring})} \quad (8)$$

Where V_{pellet} is the volume of the pellet and $t_{restructing}$ is the time when the restructuring process begins.

The total initial porosity available for migration is then:

$$p_{ini} = p^{man}_{ini} + p^{fill}_{ini} \quad (9)$$

The initial fabrication porosity and the potential volume fraction available for filling the zone between pellet fragments are assumed to be constant in the pellet. As proposed in section 3.2 we assume that the porosity velocity under the evaporation-condensation mechanism is the same for manufacturing and filling porosities. Then, if we refer to the migration equation (10)

and the mathematical demonstration proposed in section 5.2.2.1, the ratio between the filling porosity and the total porosity remains constant and is equal to its initial value γ_{ini}:

$$\frac{\partial p(x_i,t)}{\partial t} = -\mathrm{div}\left(\overrightarrow{v_p}(x_i,t)p(x_i,t)\right) \quad (10)$$

$$\frac{p^{fill}(x_i,t)}{p(x_i,t)} = \frac{p_{ini}^{fill}}{p_{ini}} = \gamma_{ini} \quad (11)$$

Where x_i are the spatial coordinates, $\overrightarrow{v_p}$ is the speed of lenticular pores associated to the volume fraction of manufacturing and filling porosities ([32], [33], [34] and [35]).

Then, knowing at each time step the central hole volume in the initial configuration (V_{hole} given by the pre-computed data of GERMINAL) and the ratio γ_{ini}, the dense volume $V_{mass\ transfer}^{fill}$ inserted between the fragments can be deduced as follows:

$$V_{mass\ transfer}^{fill}(t) = \gamma_{ini}V_{mass\ transfer}(t) = \gamma_{ini}V_{hole}(t)(1 - p_{ini}^{man}) \quad (12)$$

Finally, the restructured zone expansion transformation is derived from the parameter e giving the thickness of the volume $V_{mass\ transfer}^{fill}$ under the hypothesis of a parallelepiped shape.

$$e = \frac{1}{2Nb_{fragment}}\frac{V_{mass\ transfer}^{fill}}{h(R_{col}-R_{hole})} \quad (13)$$

where h is the fuel height, R_{col} and R_{hole} are respectively the radius of the columnar grain zone and of the central hole in the initial configuration and $Nb_{fragment}$ is the number of pellet fragments, which is equal to 8 following our geometrical assumption in section 4.1. The factor 2 comes from the symmetry of our 3D geometry. In order to obtain a better assessment of the parameter e, the radii R_{col} and R_{hole} given by GERMINAL have been upstream adjusted in order to obtain more accurate radii corresponding to experimental measurements realized in post irradiation examinations.

4.5.2. Displacement field for the relocation transformation simulation

The displacement field $\vec{u}$ used to prescribe the geometrical transformation of section 4.5.1 to the finite element mesh is defined in a cylindrical basis (u_r, u_θ, u_z) according to the following assumptions:

- Radial and axial displacements are equal to zero
- Circumferential displacement is equal to zero outside of the restructured zone

In order to avoid finite element mesh degeneration, the u_θ component is chosen to be a linear function of the polar angle θ defined as:

$$u_\theta = a\theta + b \quad (14)$$

a and b being defined such as, equation (14) respects the geometrical symmetry and the prescribed displacement defined by the parameter e in the previous section (13):

$$u_\theta(\theta = 0°) = 0 \quad (15)$$
$$u_\theta(\theta = 22.5°) = e$$

From equations (14) and (15) the displacement field in the restructured zone $[R_{hole}\,;R_{col}]$ is computed as:

$$\begin{cases} u_\theta = e * \frac{\theta}{22.5}\,, \quad \theta \in [0;22.5] \\ u_r = 0 \\ u_z = 0 \end{cases} \quad (16)$$

The displacement field $\vec{u}$, equation (16), represents the total geometrical transformation associated to the mass transfer from the beginning of irradiation. Then at each time step, an incremental transformation of the mesh coordinates is defined as follows (see illustration in Figure 9(a)).

$$\vec{x}(t_2) = \vec{x}(t_1) - \vec{u}(t_1) + \vec{u}(t_2) \quad (17)$$

with x the mesh coordinates and $(t_1;t_2)$ the beginning and the end of time step respectively. As the mesh coordinates modification (17) is made outside of the mechanical computation (Time step initialization model in Figure 7), the unilateral contact boundary condition defined on the inter-fragment plane along the restructured zone has also to be updated at the beginning of each time step with equation (18) (see Figure 9 (b)).

$$u_\theta^{tot}(r, \theta = 22.5°, t_2) = u_\theta(r, \theta = 22.5°, t_2) + u_\theta^{MEC}(r, \theta = 22.5°, t_2) \leq 0 \quad (18)$$

$$\Leftrightarrow u_\theta^{MEC}(r, \theta = 22.5°, t_2) \leq -u_\theta(r, \theta = 22.5°, t_2)$$

where u_θ^{MEC} is the circumferential displacement solution of the thermomechanical problem and u_θ the displacement prescribed to simulate the volume expansion induced by the mass transfer in the restructured zone (equation (16)).

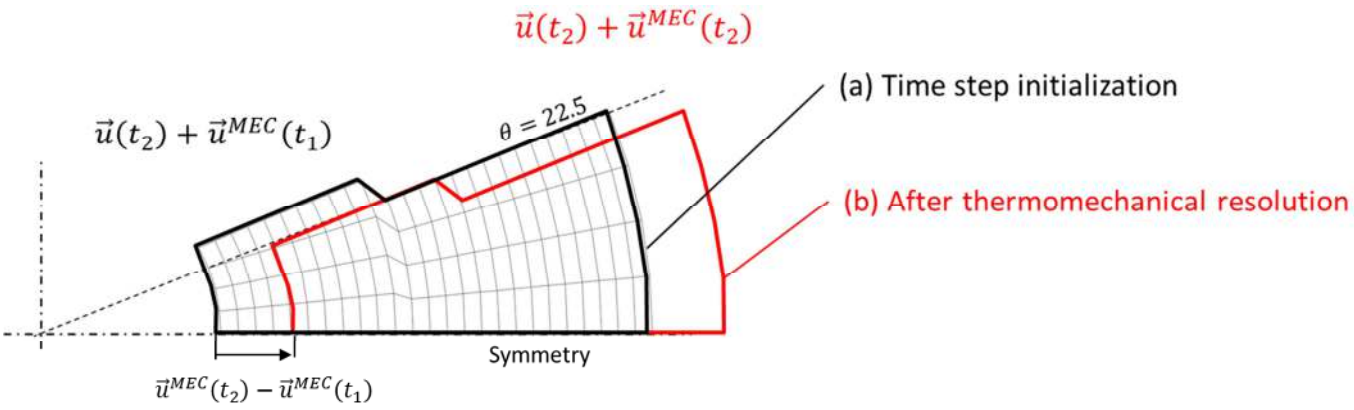

Figure 9– Illustration of the mesh transformation due to field displacement $\vec{u}$ before and after update of the unilateral condition

Thanks to this updated unilateral condition, the effect of the mass transfer transformation will induce the fuel fragment radial displacement and hence the reduction of the pellet-to-cladding gap during the mechanical resolution.

4.6. Application and results

In this section, 3D results obtained with the proposed formulation are presented in order to discuss the contribution of each radial relocation mechanism, namely fuel fragmentation and the mass transfer phenomenon. A comparison with experimental results for full and annular pellets is also proposed. These experimental results are coming from four irradiation experiments achieved in the French SFR PHENIX :

- Full pellets: fuel pin N°1 and fuel pin N°2
- Annular pellets: fuel pin N°3 and fuel pin N°4.

Irradiation history of these four pins are presented in Figure 10 with the normalized linear power evolution, and some physical data are given in Table 1. 3D simulations have been performed on these four pellets that differ from both their irradiation condition and geometry. The computation-experiment comparisons are based on the columnar grain zone radius at the end of irradiation. Indeed, this parameter is strongly correlated to the maximal temperature reached in the fuel center at the beginning of irradiation, as the migration process leading to the fuel restructuration is only activated when the temperature exceeds 1800°C. Then the validation based on this radius gives an indirect validation of the thermal computation and its coupling to other phenomena occurring under irradiation. The main objective of these comparisons is to discuss the validity of the fuel relocation and gap closure mechanisms proposed in section 3. As mentioned before, the radii of the central hole and the columnar grains zone given by GERMINAL have been adjusted upstream only in order to compute as accurately as possible

the parameter e (avoiding for example error compensation in the GERMINAL multiphysics computational scheme). Then the output columnar grain zone radius derived from the 3D computation of the temperature will enable us to assess the validity of the proposed relocation mechanisms. The final central hole radius measure has not been included in this 3D validation because this current 3D computational scheme doesn't have a migration model, and hence cannot estimate its own central hole radius.

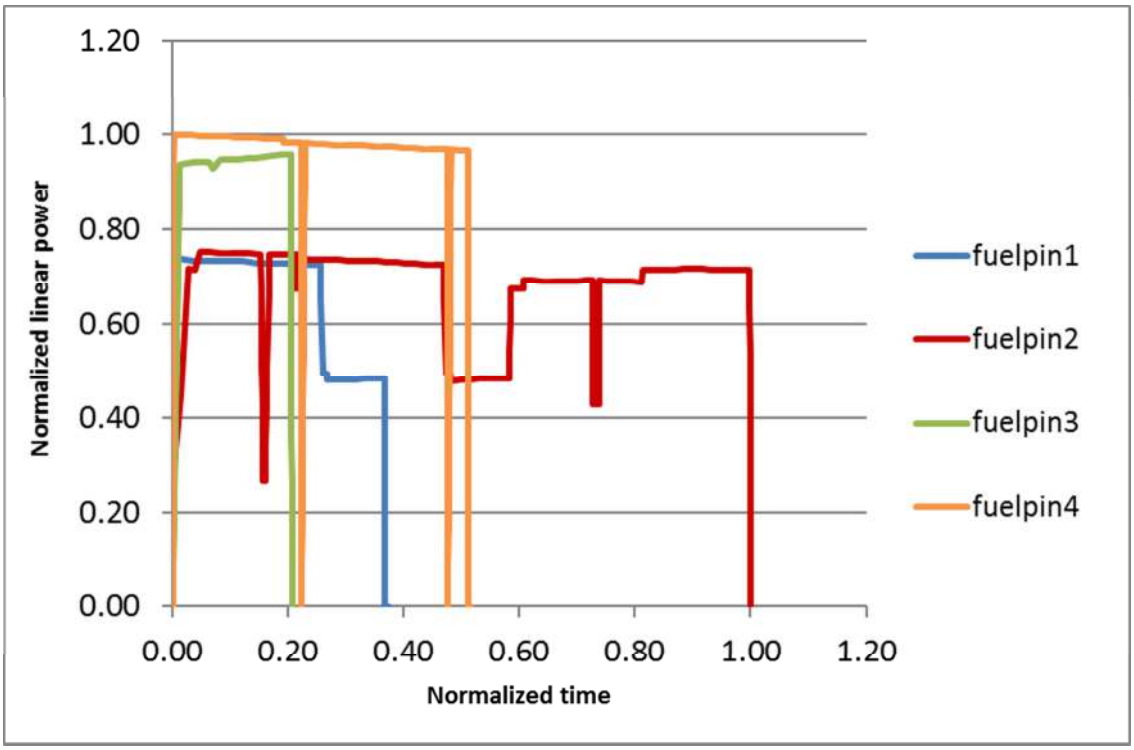

Figure 10– Normalized linear power history

	Pellet				Cladding		Coolant
	mm	mm	mm	%	mm	mm	K
Fuel pin	inner diameter	outer diameter	height	Initial porosity	inner diameter	outer diameter	temperature
1	0	2.72	12	4.4	2.82	3.27	672
2	0	2.71	12	4.3	2.82	3.27	667
3	0.98	3.65		4.4	3.75	4.32	678
4	1.03	3.56		3.6	3.68	4.25	685

Table 1: physical data of the four fuel pins

To highlight the separate impact of the two proposed mechanisms (pellet fragmentation and mass transfer), we compare the columnar grains zone radius obtained at the end of irradiation for each pin in three different cases:

- Case 1 : un-fragmented pellet under thermal gradient,
- Case 2 : fragmented pellet under a thermal gradient,
- Case 3 : fragmented pellet under a thermal gradient with the mass transfer relocation contribution.

- Hourglass effect

As explained previously (see section 3.1) the hourglass shape of the pellet lead to a variation of the pellet-to-cladding gap between the mid-pellet plane and the inter-pellet plane. In order to quantify the impact of this variation on the fuel temperature at the mid-pellet plane, we have compared the 3D results at the end of the first power increase with a fragmented pellet with

and without hourglass shape[1]. As shown in Table 2, the relative error obtained between these both cases is negligible. Then, in the following sections the relocation displacement induced by the pellet fragmentation won't consider the hourglass shape effect.

Pellet relative error	Fuelpin1	Fuelpin2	Fuelpin3	Fuelpin4
$\left(\frac{T_{hourglass}^{median-plane} - T^{median-plane}}{T_{hourglass}^{mediab-plane}}\right)$ *100	0,573%	0,574%	0,778%	1,143%
$T_{hourglass}^{median-plane}$ (Kelvin)	2616	2753	2629	2546

Table 2 : Comparison of fuel maximum temperature reached at the end of the first power increase at the median plane with and without the "hourglass effect"

- Fuel radial displacement induced by fragmentation

If we compare in Figure 11 the results for cases 1 and 2 we can observe a significant decrease of the computed columnar grain zone radius. This impact can be further analysed through the Figure 12 where during the first power increase (see linear power history in Figure 10), the pellet fragments relocation induced by the thermal gradient reduces the gap thickness in comparison with an un-fragmented pellet. This radial relocation displacement can be better observed through the 2D visualization at the median plane (see Figure 14) for a full and an annular pellet. This is due, as explained in section 3.1, to the curvature of the pellet fragment free surfaces under the radial thermal gradient. As a consequence the maximal fuel temperature reached at the end of the first power increase is lower for a fragmented pellet in comparison to an un-fragmented one (see Figure 13). But as we can see on Figure 11, despite the fragments radial relocation induced by the thermal gradient has been taken account, the columnar grain radii obtained are still too high compared to experimental measures. Indeed, the thermal gradient relocation displacement is activated only during the power increase. When the maximal power is reached, only solid swelling due to irradiation ($\dot{\bar{\varepsilon}}^{swell}$, see equation (4)) allows us to reduce the gap size, but it's negligible (cf. Figure 12). Therefore the maximal fuel temperature still increases (see Figure 13) due to the fissions gas release which tends to degrade the thermal transfer in the gap. These results show that another mechanism is needed to properly represent the gap size evolution and the fuel maximal temperature after the first power increase.

- Mass transfer impact

As we can see in Figure 11, when the mass transfer relocation mechanism is introduced (case 3), the computed restructured zone radii are in good agreement with experimental results. The maximal radius of the restructured zone is reached at the end of the first power increase, when the mass transfer just starts. After this first power increase, the mass transfer relocation displacement leads to the gap size reduction and then, by consequence, the maximal fuel temperature decrease as illustrated in Figure 12 and Figure 13. Thanks to the 3D visualization reported on Figure 15, we can observe the cracks opening in the pellet periphery due to the restructured zone volume change implemented in the 3D model (see section 4.5).

[1] To model a fragmented pellet without hourglass shape the unilateral boundary condition imposed on the inter-fragment surface ($S5_p$, see Figure 6) is changed in a symmetry boundary condition.

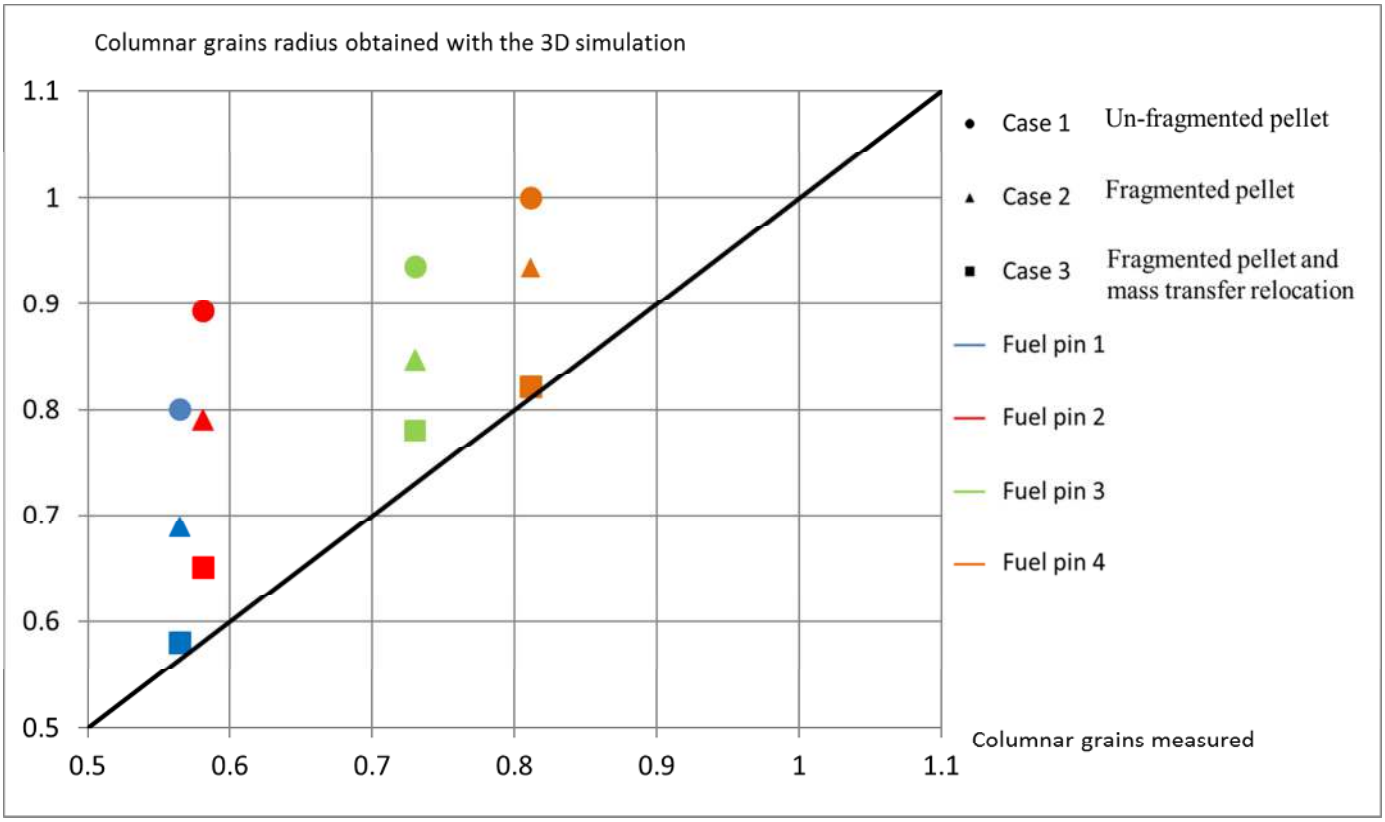

Figure 11 – Comparison of columnar grains radius between 3D finites element and experimental results (radius/3.1e-3 m on x and y axis).

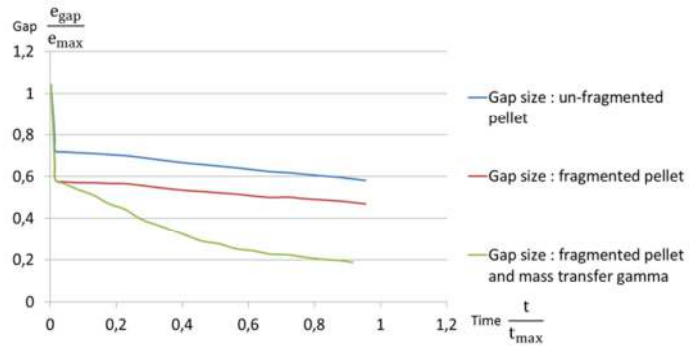

a) Fuelpin1 (e_{max} = 105µm; t_{max} = 45 days)

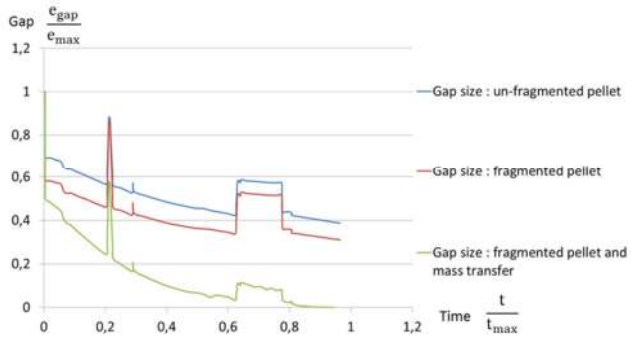

b) Fuelpin2 (e_{max} = 119µm; t_{max} = 127 days)

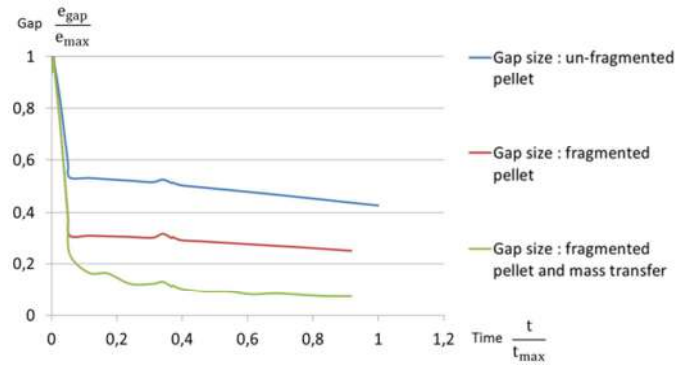

c) Fuelpin3 (e_{max} = 96.5µm; t_{max} = 35 days)

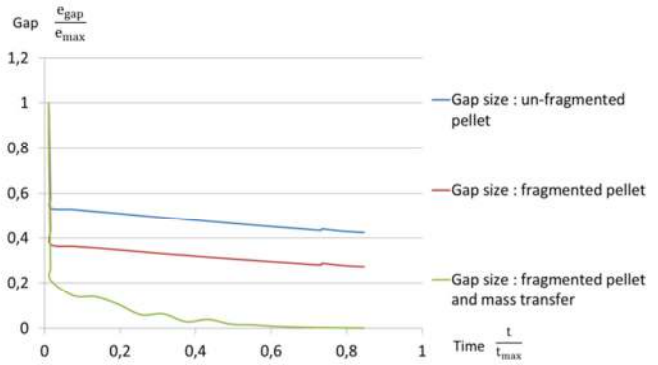

d) Fuelpin4 (e_{max} = 134µm; t_{max} = 45 days)

Figure 12 – Gap size evolution

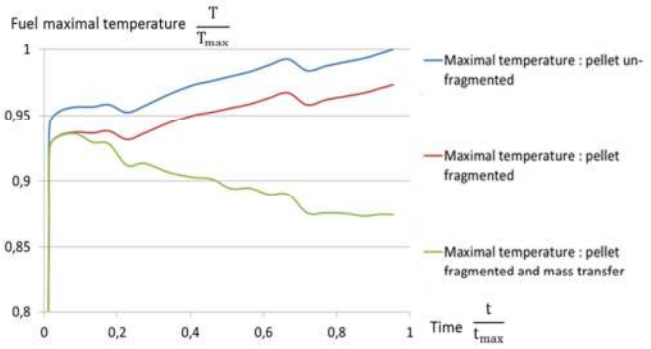

a) Fuelpin1 (T_{max} = 2845K; t_{max} = 45 days)

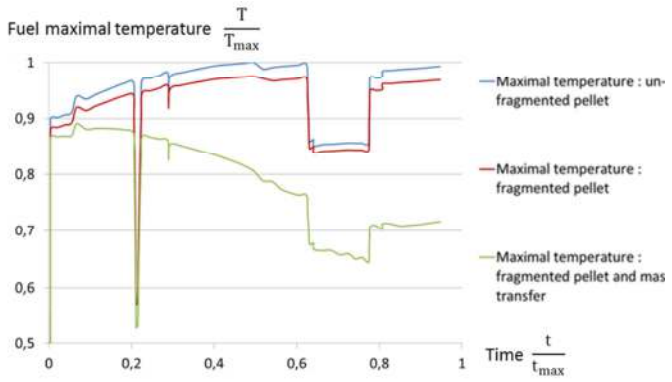

b) Fuelpin2 (T_{max} = 3095K; t_{max} = 127 days)

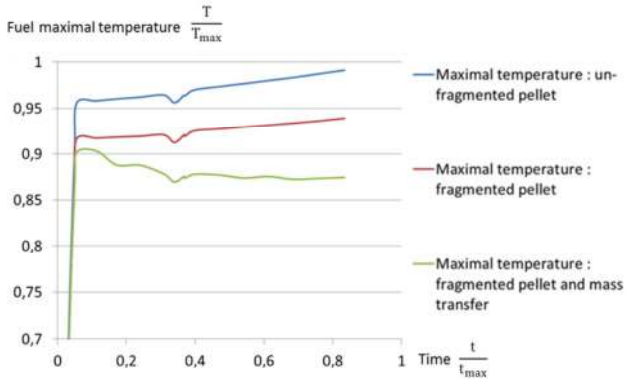

c) Fuelpin3 (T_{max} = 2817K; t_{max} = 35 days)

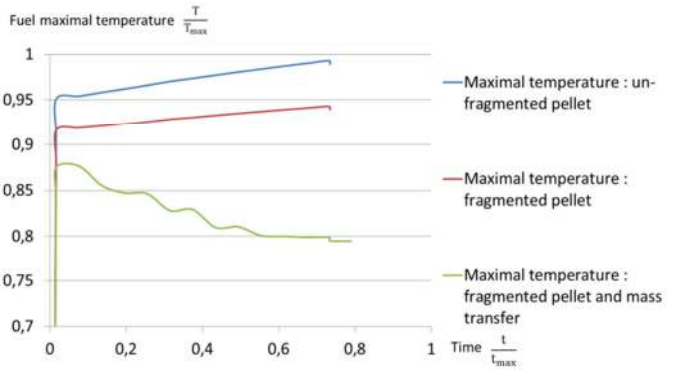

d) Fuelpin4 (T_{max} = 3005K; t_{max} = 45 days)

Figure 13 – Fuel maximum temperature evolution

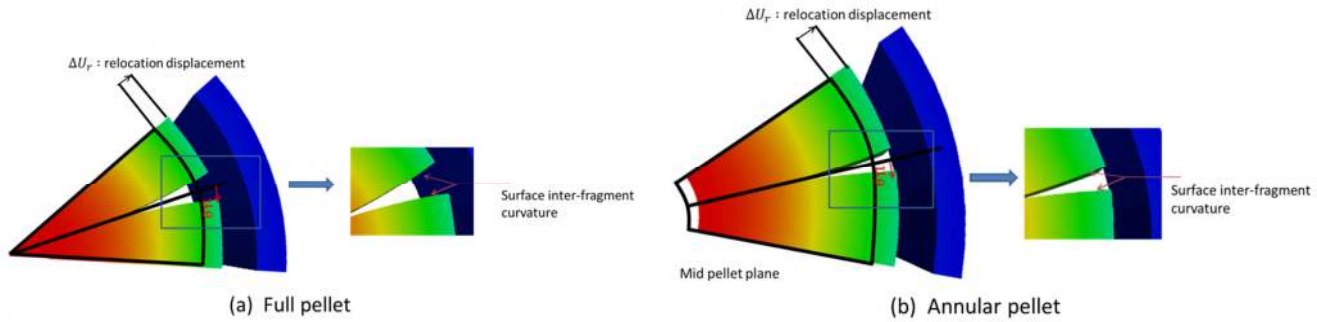

Figure 14 – Visualization of thermal gradient impact on the pellet displacement for a fragmented and an un-fragmented pellet at the median plane

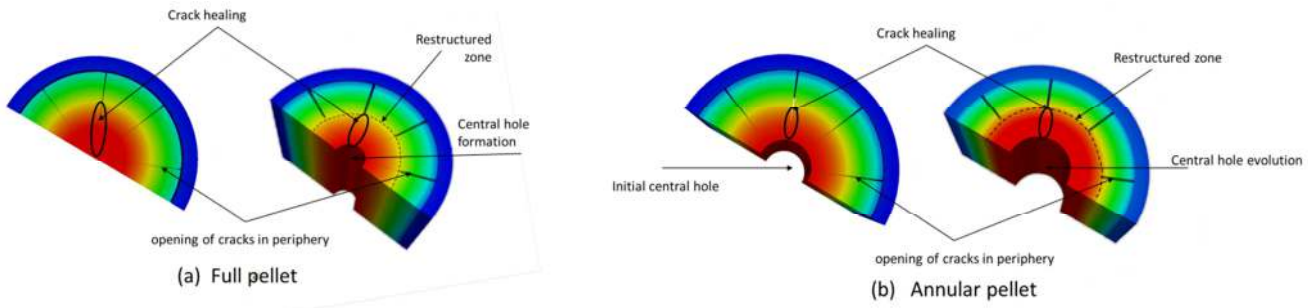

Figure 15 – Visualization of the mass transfer restructuration process

To conclude this section, 3D numerical results confirm that the pellet fragmentation relocation displacement is necessary but not sufficient to obtain a good assessment of the fuel maximal temperature. Moreover, it has been shown that the radial displacement due to the hourglass shape has a negligible effect on the temperature at the median plane and won't be consider in the sequel. The other relocation mechanism, based on the fuel mass transfer in the restructured zone as proposed in this article, improves significantly the results and gives us a physical understanding of the pellet-to-cladding gap closure phenomenon after the first power increase. Thanks to these promising results, a 1D relocation model taking separately into account the two identified phenomena is proposed in the next section.

5. NEW 1D MODEL FOR THE PELLET CLADDING GAP CLOSURE IN THE GERMINAL SFR CODE

5.1. Multi-physics coupling formulation in GERMINAL

Based on the two mechanisms highlighted in the 3D model (see section 4), a new 1D formulation of the relocation model and its coupling formulation with the GERMINAL multi-physics computational scheme have been established. The original multi-physics formulation of GERMINAL (see Figure 16 from reference [1]) has been adapted in order to replace the fuel pellet fragments relocation model and to improve its coupling formulation with fuel restructuring model (including porosities radial migration and central hole formation modellings).

Global resolutions needed by the local resolutions to come

⇒ Simplified thermal-hydraulics of coolant channel

Determines the boundary conditions for the local thermal analyses to come: cladding outer temperature in each axial slice.

N.B. Preliminary resolution for a stationary analysis only. For a transient analysis, coupled resolution with fuel pin thermal analysis.

Local resolutions ⇔ Loop on axial slices

⇒ Neutronics

⇒ Calculation of average Oxygen to Metal ratio in fuel slice *(burn-up dependent)*

⇒ Local convergence loop

→ Thermal analysis of fuel and cladding

Coupled with coolant thermal-hydraulics for a transient analysis

→ Thermally activated fuel physical processes

~ Oxygen radial migration *with specific update frequency*

~ Fuel irradiation shrinkage

~ Fuel swelling *(gas and solid swelling)*

~ Fuel pellet fragments relocation

~ Gaseous and volatile fission products behavior

Includes "Joint Oxyde-Gaine" formation.

→ Mechanics of fuel and cladding

⇒ Oxygen potential calculation *with specific update frequency*

⇒ Major actinides radial redistribution *with specific update frequency*

⇒ Fuel restructuring: porosities radial migration and central hole formation *with specific update frequency*

Global resolutions needing the previous local resolutions

⇒ Plenum gas composition and pressure

⇒ Fuel column axial relocation

⇒ Cladding internal and external corrosion

⇒ Fuel column compression spring reaction

Figure 16 - One-time step resolution by GERMINAL [1]

This new formulation is explained below through equations (19), (20), (21) and (22).

Heat equation

$$\rho c_p \frac{\partial T(\vec{u}^{mec}, p)}{\partial t} = \mathrm{div}\left(\lambda(p)\overrightarrow{\mathrm{grad}}T(\vec{u}^{mec}, p)\right) + p_v \tag{19}$$

Migration/advection equation

$$\frac{\partial p(T)}{\partial t} = -\mathrm{div}\left(\overrightarrow{v_p}(T)p(T)\right) \tag{20}$$

Relocation strain equation

$$\bar{\bar{\varepsilon}}^{relocation}(T, p) = \bar{\bar{\varepsilon}}^{relocation}_{frag}(T) + \bar{\bar{\varepsilon}}^{relocation}_{mass\ transfer}(p) \tag{21}$$

Static mechanical equilibrium equation and boundary conditions

$$\begin{cases} \mathrm{div}\bar{\bar{\sigma}} = 0 \text{ in } \Omega \\ \bar{\bar{\sigma}}\,\vec{n} = \vec{\Sigma}_{imp} \text{ on } \partial\Omega_T \\ \vec{u}^{mec} = \vec{U}_{imp} \text{ on } \partial\Omega_u \end{cases} \tag{22}$$

such as, $\partial\Omega_T \cap \partial\Omega_u = \emptyset$ and $\partial\Omega_T \cup \partial\Omega_u = \partial\Omega$

with the following constitutive law :

$$\dot{\bar{\bar{\sigma}}} = \underline{\underline{\underline{\underline{E}}}} : \left(\dot{\bar{\bar{\varepsilon}}}^{tot}(\vec{u}^{mec}) - \dot{\bar{\bar{\varepsilon}}}^{th}(T) - \dot{\bar{\bar{\varepsilon}}}^{plast}(T, p) - \dot{\bar{\bar{\varepsilon}}}^{creep}(T, p) - \dot{\bar{\bar{\varepsilon}}}^{swell}(T) - \dot{\bar{\bar{\varepsilon}}}^{relocation}(T, p)\right)$$

If the node is localized in the central hole:

$$\begin{cases} \bar{\bar{\sigma}} = 0 \\ \overrightarrow{v_p} = 0 \end{cases} \tag{23}$$

with ρ is the density (g/m^3), c_p the heat capacity (J/K), λ the thermal conductivity ($W/m.K$), p_v the local nuclear power density (W/m^3), p the volume fraction of porosity (manufacturing and filling porosities), $\overrightarrow{v_p}$ is the average migration speed of pores coming from both manufacturing and filling volume ([32], [33], [34] and [35]), $\vec{u}^{mec}$ is the mechanical displacement field, $\bar{\bar{\varepsilon}}^{relocation}_{frag}$ and $\bar{\bar{\varepsilon}}^{relocation}_{mass\ transfer}$ are the relocation strains related respectively to the pellet fragmentation and to the mass transfer. As we can see the constitutive equations (19)-(23) are directly or indirectly coupled to each other mainly through the variables T, p and $\vec{u}^{mec}$ as following :

- the kinetic of pores migration is controlled by the temperature.
- the relocation strain related to the mass transfer and to the pellet fragmentation depends on the pore volume fraction and on the temperature respectively.
- the mechanical displacement depends on the relocation strain, the temperature and porosity through the inelastic strains.
- the thermal state depends on the mechanical displacement and the porosity via the pellet-to-cladding gap heat exchange and the thermal properties .

The new fuel pellet fragments relocation model and its coupling formulation with the porosities radial migration and central hole formation models are detailed in the following sections.

5.2. New Fuel pellet fragments relocation model and coupling formulation.

As discussed in sections 3 and 4, the new relocation model is composed of two strains (see equation (21)), one related to the impact of the thermal gradient on a fragmented pellet and the second one related to the impact of the mass transfer in the restructuring zone. In the following sections, constitutive equations of these relocation strains are presented.

5.2.1. Relocation strain induced by the pellet fragmentation

5.2.1.1. Mechanical formulation

The pellet "hourglass" effect is not considered in our 1D model. Indeed, as illustrated in section 4.6 (results in Table 2) its effect on the temperature is negligible at the mid plane where the maximal temperature is reached. Then the fragmentation relocation strain describe the radial displacement induced by the contact between pellet fragments (see Figure 2)

The fragmentation relocation strain is assessed thanks to the difference of the displacements (namely "ΔU_r" in Figure 2) between an un-fragmented and a fragmented pellet submitted to a thermal gradient. In our approach, we have considered initial full and annular pellets with the following assumptions:

- 2D representation in the (r, θ) plane.
- Isotropic elastic behaviour
- No external forces, only thermal loading

Each radial displacement "U_r" is obtained by solving a mechanical system (24) with a displacement approach for the fragmented and un-fragmented pellet, considering an annular and a full geometry for both.

$$\begin{aligned} &\mathrm{div}\ \bar{\bar{\sigma}} = 0 \\ &\bar{\bar{\sigma}} = 2G\left(\frac{\nu}{1-2\nu}\mathrm{tr}\left(\bar{\bar{\varepsilon}} - \bar{\bar{\varepsilon}}^{th}\right)\bar{\bar{I}} + \left(\bar{\bar{\varepsilon}} - \bar{\bar{\varepsilon}}^{th}\right)\right) \\ &\bar{\bar{\varepsilon}} = \frac{1}{2}\left(\overline{\overline{\mathrm{grad}}}(\vec{u}) + \overline{\overline{\mathrm{grad}}}^{T}(\vec{u})\right) \end{aligned} \tag{24}$$

where G and ν denote the shear modulus and the Poisson's ratio of the pellet, $\bar{\bar{\varepsilon}}$ and $\bar{\bar{\varepsilon}}^{th}$ are respectively the total strain tensor and the thermal strain tensor, $\vec{u}$ is the displacement field and $\bar{\bar{\sigma}}$ the stress tensor.

Thermal strains are introduced through a stress free strain field $\bar{\bar{\varepsilon}}^{th}(r)$ defined in equations (25) and (26) for an annular and a full pellet under steady state thermal condition.

$$\begin{aligned} \bar{\bar{\varepsilon}}^{th}_{full}(r) &= \alpha(T_{full}(r) - T_0)\bar{\bar{I}} = \hat{\varepsilon}^{th}_{full}(r)\bar{\bar{I}} + \tilde{\varepsilon}^{th}_{full}(r)\bar{\bar{I}} \\ \bar{\bar{\varepsilon}}^{th}_{an}(r) &= \alpha(T_{an}(r) - T_0)\bar{\bar{I}} = \hat{\varepsilon}^{th}_{an}(r)\bar{\bar{I}} + \tilde{\varepsilon}^{th}_{an}(r)\bar{\bar{I}} \end{aligned} \tag{25}$$

where $T_{full}(r)$ and $T_{an}(r)$ are respectively the radial temperature field for a full and a annular pellet, T_0 is the initial temperature of the pellet with a uniform spatial distribution, α is the thermal expansion coefficient, $\bar{\bar{I}}$ is the unit second order tensor, $\left(\hat{\varepsilon}^{th}_{full}(r), \hat{\varepsilon}^{th}_{an}(r)\right)$ and $\left(\tilde{\varepsilon}^{th}_{full}(r), \tilde{\varepsilon}^{th}_{an}(r)\right)$ are respectively the non harmonic and the harmonic distribution of the thermal strains for a full pellet and annular pellet. The splitting of the stress-free strain field to a nonharmonic and harmonic distribution is imposed by the resolution method of the fragmented pellet problem. In the latter the total displacement is derived from the sum of two analytical solutions : one for an harmonic stress free strain and the other one for a nonharmonic stress free strain (see equations (A- 8) and (A- 9) in Appendix 2).

$$\hat{\varepsilon}^{th}_{full}(r) = \varepsilon_3^{full} r^2$$
$$\tilde{\varepsilon}^{th}_{full} = \varepsilon_1^{full} \quad (26)$$
$$\text{such as :} \begin{cases} \varepsilon_3^{full} = -\frac{\alpha\left(T^{full}(0) - T^{full}(R_e)\right)}{Re^2} \\ \varepsilon_1^{full} = -\varepsilon_3^{full} R_e^2 + \alpha(T^{full}(R_e) - T_0) \end{cases}$$

$$\hat{\varepsilon}^{th}_{an}(r) = \varepsilon_3^{an} r^2$$
$$\tilde{\varepsilon}^{th}_{an}(r) = \varepsilon_2^{an} \ln(r) + \varepsilon_1^{an} \quad (27)$$
$$\text{such as :} \begin{cases} \varepsilon_3^{an} = -\frac{\alpha\left(T^{an}(R_i) - T^{an}(R_e)\right)}{\left(R_e^2 - R_i^2 + 2R_i^2 \ln\left(\frac{R_i}{R_e}\right)\right)} \\ \varepsilon_2^{an} = -2\varepsilon_3^{an} R_i^2 \\ \varepsilon_1^{an} = -\varepsilon_3^{an}(R_e^2 - 2R_i^2 \ln(R_e)) + \alpha(T^{an}(R_e) - T_0) \end{cases}$$

Where R_e and R_i are respectively the external and internal radius of the pellet.

5.2.1.2. Un-fragmented pellet

By considering an axisymmetric problem for the un-fragmented pellet, we find the following analytical solution (equations (28) and (29)).

$$u_r^{full-axi}(r) = \left(\frac{1}{1-\nu}\right)\frac{1}{r}\int_0^r t\left(\varepsilon_1^{full} + \varepsilon_3^{full} t^2\right)dt + ar \quad (28)$$

$$u_r^{an-axi}(r) = \left(\frac{1}{1-\nu}\right)\frac{1}{r}\int_{R_i}^r t(\varepsilon_1^{an} + \varepsilon_2^{an}\ln(t) + \varepsilon_3^{an} t^2)dt + \frac{b}{r} + cr \quad (29)$$

where a, b and c are given by the boundary conditions such as the radial stress on the pellet periphery ($r = R_e$) and, for annular pellet, at the pellet centre ($r = R_i$) equals zero:

Full pellet:

- $\sigma_{rr}^{full-axi}(R_e) = 0$

Annular pellet:

- $\begin{cases} \sigma_{rr}^{an-axi}(R_e) = 0 \\ \sigma_{rr}^{an-axi}(R_i) = 0 \end{cases}$

where, σ_{rr}^{an-axi} and $\sigma_{rr}^{full-axi}$ are respectively annular and full pellet radial stresses derived from the thermo elastic law given in equation (24) (see Appendix 1 for the expression of the stress tensor components and the constants a, b and c).

5.2.1.3. Fragmented pellet

For the fragmented pellet, where the axisymmetric condition is no more valid, the approach proposed by Muskhelishvili [36] has been extended. The radial component of the displacement field for a full pellet has already been determined by Sercombe and al. [37], using the Muskhelishvili approach[2] (see Appendix 2 for development):

$$u_r^{full-frag}(r,\theta) = \varepsilon_3^{full}\left[\left(\frac{1}{1-\nu}\right)\frac{1}{r}\left(\int_0^r t^3 dt\right) - \frac{1}{2G}\left[4\nu\gamma^{full}(G,\nu)\cos(2\theta) + \beta^{full}(G,\nu)\cos(4\theta)\right]r^3\right] \quad (30)$$
$$+ \varepsilon_1^{full} r + \frac{A}{2G}\left[(4-4\nu)\cos(\theta)\ln\left(\frac{r}{r_0}\right) + (2-4\nu)\theta\sin(\theta) - \cos(\theta)\right]$$

[2] for the sake of completeness the analytical developments for a full pellet are given again in the present paper

As explained in [37], the displacement field is singular at the apex of the full pellet (see function $\ln\left(\frac{r}{r_0}\right)$ with $r_0 > 0$ in equation (30)) and is not consistent with the boundary condition $u_r^{full-frag}(0,\theta) = 0$. To overcome this, the latter is approximated through equation (31) where the parameter r_0 is defined in order to have the same boundary condition for the average radial displacement at a small radius $r = r_i$ (see Appendix 3 for developments). Then, due to this approximation the displacement field doesn't have a physical meaning when the radius is lower than r_i.

$$\frac{1}{2\theta_m}\int_{-\theta_m}^{\theta_m} u_r^{full-frag}(r_i,\theta)d\theta = 0 \quad (31)$$

where, $\theta_m = 22.5°$ and $r_i \ll R_e$.

Based on works established in [37], we have proposed a new solution for an annular pellet (see Appendix 2 for development):

$$u_r^{an-frag}(r,\theta) = \varepsilon_3^{an}\left[\left(\frac{1}{1-\nu}\right)\frac{1}{r}\left(\int_{R_i}^{r} t^3 dt\right) - \frac{1}{2G}[4\nu\gamma^{an}(G,\nu)\cos(2\theta) + \beta^{an}(G,\nu)\cos(4\theta)]r^3\right] + \varepsilon_1^{an} r + \varepsilon_2^{an} r(\ln(r) - 1) + \frac{d}{r} + \frac{B}{2G}\left[(4-4\nu)\cos(\theta)\ln\left(\frac{r}{R_i}\right) + (2-4\nu)\theta\sin(\theta) - \cos(\theta)\right] \quad (32)$$

In the previous equation (30) and (32) $\gamma^{full}, \beta^{full}, A, \gamma^{an}, \beta^{an}, d$ and B are the integration constants derived from the following boundary conditions, equations (33) to (36), for the stress components (see Appendix 3 for developments of these boundary conditions).

As explained in reference [37] the stress field is not rigorously statically admissible then the boundary conditions for constants A, B and d are defined such as the average radial stress on the pellet external radius ($r = R_e$) and on the annular pellet internal radius ($r = R_i$) equals zero :

Full pellet:

$$\frac{1}{2\theta_m}\int_{-\theta_m}^{\theta_m} \sigma_{rr}^{full-frag}(R_e,\theta)d\theta = 0 \quad (33)$$

Annular pellet:

$$\frac{1}{2\theta_m}\int_{-\theta_m}^{\theta_m} \sigma_{rr}^{an-frag}(R_e,\theta)d\theta = 0 \quad (34)$$

$$\frac{1}{2\theta_m}\int_{-\theta_m}^{\theta_m} \sigma_{rr}^{an-frag}(R_i,\theta)d\theta = 0$$

Constants γ^{full}, β^{full}, γ^{an} and β^{an} are calculated by considering the following boundary conditions on the pellet fragment free surface ($\theta = \pm\theta_m$):

Full pellet:

$$\begin{cases}\sigma_{r\theta}^{full-frag}(r,\pm\theta_m) = 0\\ \sigma_{\theta\theta}^{full-frag}(r,\pm\theta_m) = 0\end{cases} \text{ for } r_i \le r \le R_e \quad (35)$$

Annular pellet:

$$\begin{cases}\sigma_{r\theta}^{an-frag}(r,\pm\theta_m) = 0\\ \frac{1}{(R_e-R_i)}\int_{R_i}^{R_e}\sigma_{\theta\theta}^{an-frag}(r,\pm\theta_m) = 0\end{cases} \text{ for } R_i \le r \le R_e \quad (36)$$

As mentioned previously the stress field is not rigorously statically admissible, then the boundary condition of the annular pellet circumferential stress is modified in order to obtain an average value equals to zero on the pellet free surface.

5.2.1.4. Relocation strain

To establish the relocation strain, the difference of displacement between a fragmented and an un- fragmented pellet is first assessed (see Appendix 4 step 1). As we consider the assumption of a homogeneous relocation strain [1], the latter is derived from the difference of the maximal displacement, that means at $r = R_e$ and $\theta = \frac{\pi}{8}$ (see Appendix 4 step 2).

Finally, if we consider displacement solutions given in sections 5.2.1.2 and 5.2.1.3 with constant values substitution (see Appendix 4 step 3), then the radial displacement differences are:

$$\Delta u_r^{full}\left(R_e, \frac{\pi}{8}\right) = -k_{full}\varepsilon_3^{full}{R_e}^3 \quad (37)$$

$$\Delta u_r^{an}\left(R_e, \frac{\pi}{8}\right) = -k_{an}\varepsilon_3^{an} \quad (38)$$

Where k_{full} and k_{an} depends on the material and the geometry and are defined in Appendix 4.

We can finally obtain the relocation strain tensor expression related to the pellet fragmentation as a function of the thermal expansion for a full and annular pellet (see expressions of ε_3^{full} and ε_3^{an} respectively in the equations (26) and (27)):

$$\bar{\bar{\varepsilon}}_{frag-full}^{relocation} = \frac{\Delta u_r^{full}\left(R_e, \frac{\pi}{8}\right)}{R_e}\ (\vec{e}_r \otimes \vec{e}_r + \vec{e}_\theta \otimes \vec{e}_\theta) = k_{full}\alpha(\,T^{full}(0) - T^{full}(R_e))(\vec{e}_r \otimes \vec{e}_r + \vec{e}_\theta \otimes \vec{e}_\theta) \quad (39)$$

$$\bar{\bar{\varepsilon}}_{frag-an}^{relocation} = \frac{\Delta u_r^{an}\left(R_e, \frac{\pi}{8}\right)}{R_e}\ (\vec{e}_r \otimes \vec{e}_r + \vec{e}_\theta \otimes \vec{e}_\theta) = k_{an}\frac{\alpha(\,T^{an}(R_i) - T^{an}(R_e))}{\left(R_e^2 - R_i^2 + 2R_i^2 \ln\left(\frac{R_i}{R_e}\right)\right).R_e}(\vec{e}_r \otimes \vec{e}_r + \vec{e}_\theta \otimes \vec{e}_\theta) \quad (40)$$

Modification of this solution has been proposed (see equations (41) and (42)) in order to take into account the thermo-mechanical nonlinear behaviour of the fuel pellet during irradiation. This is done by introducing an empirical parameter k_{fit} which depends on the creep and plasticity material behaviour and should be equal to one in the elastic case. This empirical parameter k_{fit} has then been fitted on the 3D finite element simulation for the fuel material properties proposed in GERMINAL [1] in the case of an annular and a full pellet under the first power increase. This k_{fit} parameter needs to be adjusted for each new non linear behaviour law of the pellet. This 3D simulation is based on the computational scheme described in section 4.3.

$$\bar{\bar{\varepsilon}}_{frag-full}^{relocation} = k_{fit}k_{full}\alpha\left(T^{full}(0), {}^{O}/_{M}(0)\right)(\,T^{full}(0) - T^{full}(R_e))\ (\vec{e}_r \otimes \vec{e}_r + \vec{e}_\theta \otimes \vec{e}_\theta) \quad (41)$$

$$\bar{\bar{\varepsilon}}_{frag-an}^{relocation} = k_{fit}k_{an}\frac{\alpha\left(T^{an}(R_i), {}^{O}/_{M}(R_i)\right)(\,T^{an}(R_i) - T^{an}(R_e))}{\left({R_e}^2 - {R_i}^2 + 2{R_i}^2 \ln\left(\frac{R_i}{R_e}\right)\right)R_e}\ (\vec{e}_r \otimes \vec{e}_r + \vec{e}_\theta \otimes \vec{e}_\theta) \quad (42)$$

The fuel thermal expansion coefficient is temperature and oxygen to metal ratio dependant [1]. The analytical solutions of equations (39) and (40) consider a constant thermal expansion coefficient. To be consistent with this assumption, the value proposed in equations (41) and (42) is defined at the inner pellet radius. This choice gives the best fit of parameter k_{fit} between the 3D finite element results (where the thermal expansion coefficient is temperature and O/M ratio dependent) and the analytical solution. On Figure 17 we can see the good agreement between the analytical relocation strain and the relocation strain derived from the displacement field computed in the 3D simulation.

$$\frac{\varepsilon_{rr}^{relocation}}{\varepsilon_{max}^{an}} = \frac{\varepsilon_{\theta\theta}^{relocation}}{\varepsilon_{max}^{an}}$$

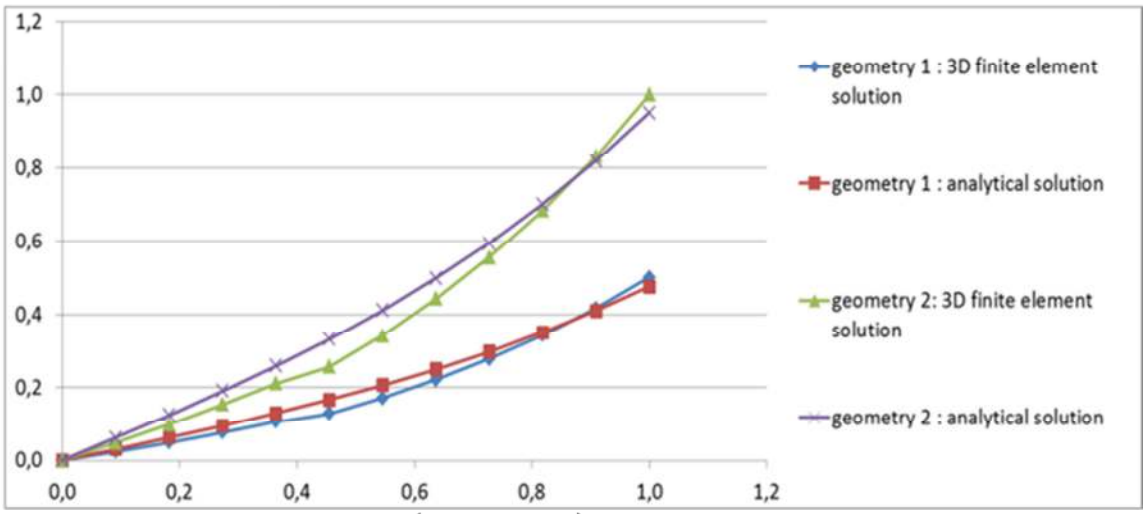

.

a) Annular pellet ($\varepsilon_{max}^{an} = 1.58e-2$; $\Delta T_{max}^{an} = 1300K$)

$$\frac{\varepsilon_{rr}^{relocation}}{\varepsilon_{max}^{full}} = \frac{\varepsilon_{\theta\theta}^{relocation}}{\varepsilon_{max}^{full}}$$

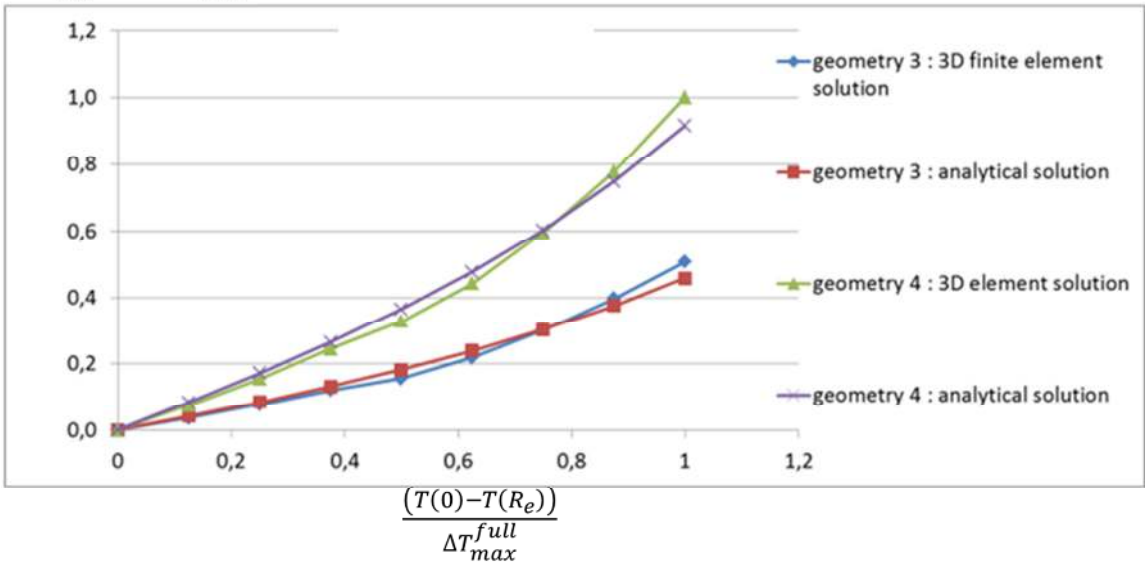

b) Full pellet ($\varepsilon_{max}^{full} = 5.5e-3$; $\Delta T_{max}^{full} = 1256K$)

Figure 17 Relocation strain evolution related to the pellet fragmentation in function of thermal dilatation for different geometries: geometry 1 ($R_i = 0.9775mm$; $R_e = 3.65mm$), geometry 2 ($R_i = 1.955mm$; $R_e = 7.3mm$), geometry 3 ($R_i = 0mm$; $R_e = 2.72mm$) and geometry 4 ($R_i = 0mm$; $R_e = 5.44mm$).

5.2.2. Mass transfer relocation strain

As presented in section 3.2 and verified with 3D modelling in section 4, a relocation strain induced by the mass transfer has to be assessed in this new 1D relocation model.

5.2.2.1. Computation of the transferred mass

The transferred mass can be derived from the porosity migration phenomenon thanks to the advection equation (20). In the latter p is the total porosity including both manufacturing and filling porosities.

$$p(r,t) = p^{man}(r,t) + p^{fill}(r,t) \tag{43}$$

As already introduced in section 4.5.1 the ratio between the filling porosity and the total porosity writes

$$\gamma(r,t) = \frac{p^{fill}(r,t)}{p(r,t)} \tag{44}$$

Moreover it is assumed that its initial value is not radius dependent: $\gamma(r,0) = \gamma_{ini} = \frac{p_{ini}^{fill}}{p_{ini}}\ \forall\, r$

The new advection equation solved is then:

$$\begin{cases} \frac{\partial p(r,t)}{\partial t} = -\mathrm{div}\left(\overrightarrow{v_p}(r,t)p(r,t)\right) \\ p(r,0) = p_{ini}^{man} + p_{ini}^{fill} \end{cases} \qquad \forall\, r \in R+ \text{ and } \forall\, t \geq 0 \tag{45}$$

Where $\overrightarrow{v_p}(r,t)$ is the speed of l lenticular pores associated to the volume fraction of manufacturing and filling porosities ([32], [33], [34] and [35]).

The central hole size evolution during irradiation is derived from solution of equation (45) as follows:

$$V_{Hole}(t) = \int_V H(p(r,t))dv \tag{46}$$

$$\text{such as : } \begin{cases} H\left(p(r,t)\right) = 1 & \text{if } p(r,t) = p_{max} \\ H(p(r,t)) = 0 & \text{if } p(r,t) < p_{max} \end{cases}$$

Where p_{max} is the maximal porosity (close to 100%) imposed on the solution of the advection equation (45). In the latter the pores velocity $v_p(r,t)$ is set to zero when $p = p_{max}$.

To assess the dense volume transferred between pellet fragments (see $V_{mass-transfer}^{fill}$ in Figure 8), we need to compute the proportion of the central hole volume coming from the filling porosities. Then the volume $V_{mass-transfer}^{fill}$ is defined thanks to equation (47) where we consider only the filling porosity and the initial dense volume located in the central hole:

$$V_{mass-transfer}^{fill}(t) = \int_V H(p^{fill}(r,t))(1 - p_{ini}^{man})dv \tag{47}$$

The evolution of $p^{fill}(r,t)$, needed to compute $V_{mass-transfer}^{fill}(t)$, is derived from the assumption that filling and manufacturing porosities have the same migration velocity. Then the filling porosity $p^{fill}(r,t)$ is the solution of the following advection problem (48).

$$\begin{cases} \frac{\partial p^{fill}(r,t)}{\partial t} = -\mathrm{div}\left(v_p(r,t)p^{fill}(r,t)\right) \\ p^{fill}(r,0) = p_{ini}^{fill} \end{cases} \tag{48}$$

To avoid solving two advection problems ((45) and (48)), according to the Cauchy-Lipschitz theorem, advection equation of type (45) or (48) admits a unique solution $p \in C^1$ given by the following formula[39]:

$$p(R(r_{ini},t),t) = J^{-1}(r_{ini},t)p_{ini} \quad (49)$$

$$\text{with: } \begin{cases} J(r_{ini},t) = e^{\int_0^t \text{div}\, v_p(R(r_{ini},t),s)\, ds} \\ J(r_{ini},t=0) = 1 \\ R(r_{ini},t) = r \end{cases}$$

such as: $r_{ini} \in R+ \rightarrow R(r_{ini},t) \in R+$ is the application called flow and $J(r_{ini},t)$ is the Jacobian of characteristic flow [39]. The flow is defined thanks to the characteristics of the advection equation:

$$\begin{cases} \dot{R} = v_p(R(t,r_{ini}),t) \\ R(r_{ini},t=0) = r_{ini} \end{cases} \quad (50)$$

According to equations (49) the solution p^{fill} of equation (48) writes:

$$p^{fill}(r,t) = J^{-1}(r_{ini},t)\gamma_{ini}p_{ini} \Leftrightarrow \frac{p^{fill}(r,t)}{\gamma_{ini}} = J^{-1}(r_{ini},t)p_{ini} \quad (51)$$

By the same way, we deduce the analytic solution $p(r,t)$ of equation (45):

$$p(r,t) = J^{-1}(r_{ini},t)p_{ini} \quad (52)$$

By identification we can conclude that:

$$p^{fill}(r,t) = \gamma_{ini}p(r,t) \quad (53)$$

According to equations (47) and (53), we can finally deduce the expression of $V^{fill}_{mass\ transfer}$ as a function of V_{Hole}:

$$V^{fill}_{mass-transfer}(t) = \int_V H(\gamma_{ini}p(r,t))(1 - p^{man}_{ini})dv \quad (54)$$
$$\Leftrightarrow V^{fill}_{mass-transfer}(t) = \gamma_{ini}V_{Hole}(t)\,(1 - p^{man}_{ini})$$

When the gap is closed, if the mass transfer is still active this will lead to a compression stress in the pellet fragment due to the increasing volume of the restructuring zone. This phenomenon, which would lead to pellet cladding mechanical interaction at the beginning of irradiation, has not been observed in post irradiation examination. To prevent this artificial mechanical interaction the porosity migration process must be completed in order to have reached the maximal value of $V^{fill}_{mass\ transfer}$ when the gap is closed. Due to the simplifications of the filling porosity migration process, this stop mechanism cannot be ensured for all irradiation conditions in the present model.

5.2.2.2. Relocation strain induced by mass transfer

It is now possible to compute the relocation strain thanks to the volume expansion induced by the mass transfer « $V^{fill}_{mass\ transfer}$ » in the restructuring zone « V_{restr} » as described in sections 3.2 and 4.5.1 :

$$\varphi^{relocation}_{mass-transfer} = \int_{V_0}^{V_1} \frac{dV}{V} = \ln\left(\frac{V_1}{V_0}\right) \quad (55)$$

$$\text{such as : } \begin{cases} V_1 = V_0 + V^{fill}_{mass\ transfer} \\ V_0 = V_{restr} \end{cases}$$

Where $\varphi^{relocation}_{mass-transfer}$ is the volume expansion ratio of the restructuring zone, V_0 and V_1 correspond respectively to the volume of the restructuring zone before and after the mass transfer (see Figure 18). In order to consider only the transformation due to the mass transfer in the finite strain computation of the relocation transformation, the volumes V_1 and V_0 are assessed on an initial geometrical configuration (without considering the mechanical displacement). The volume of the restructuring zone V_{restr} is given by a temperature criterion $T > T_{restr}$ (here $T_{restr} = 1800°C$).

The relocation strain is assumed to be homogeneous in the plane (r, θ), then the expression of the tensor $\bar{\bar{\varepsilon}}^{relocation}_{mass-transfer}$ is given as follows:

$$\bar{\bar{\varepsilon}}^{relocation}_{mass-transfer} = \frac{1}{2}\varphi^{relocation}_{mass-transfer}\ (\vec{e}_r \otimes \vec{e}_r + \vec{e}_\theta \otimes \vec{e}_\theta) \tag{56}$$

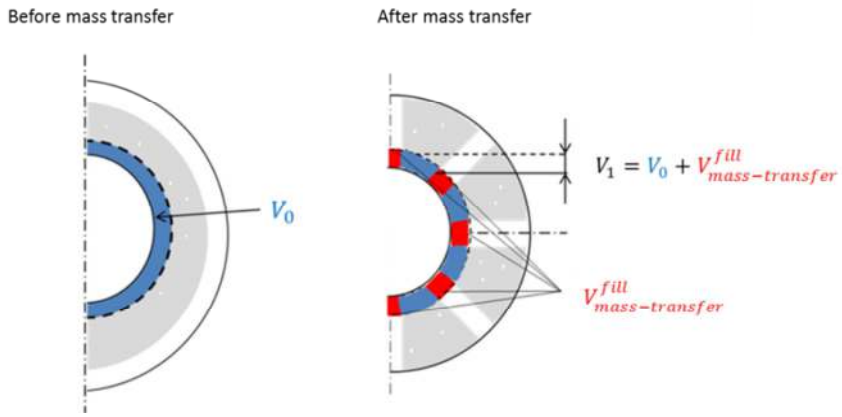

Figure 18– Illustration of the change of volume of the UPuO2 matrix generated by the mass transfer occurring between the fragments in the restructuring zone.

We finally obtain the following coupling formulation between the relocation strain and the mass transfer occurring during the central hole formation:

$$\begin{cases} \bar{\bar{\varepsilon}}^{relocation}_{mass-transfer} = \frac{1}{2}\ln\left(\frac{V_{restr}+V^{fill}_{mass\ transfer}}{V_{restr}}\right)(\vec{e}_r \otimes \vec{e}_r + \vec{e}_\theta \otimes \vec{e}_\theta) \\ V^{fill}_{mass\ transfer} = \gamma_{ini} V_{hole}(1 - p^{man}_{ini}) \end{cases} \tag{57}$$

Where the parameters $V_{restr}, \gamma_{ini}, V_{hole}$ and p^{man}_{ini} can be respectively found in the equation (55), (44), (45) and (46).

According to equation (21), the total relocation strain is obtained by summing equations (41) and (57) for full pellet configuration and equations (42) and (57) for annular pellet configuration.

5.3. Results and comparisons with experimental measurements

The objective of this section is to illustrate the results and the validity of this new relocation model implemented in GERMINAL. Then, the same annular and full pellets as those introduced in section 4.6 have been considered. Central hole and columnar grain zone radii obtained at the end of irradiation with the new coupling scheme have been compared to those obtained with the previous version of GERMINAL but also to experimental measurements.

Figure 19 illustrates our new results regarding the coupling between central hole radius, gap size and fuel maximal temperature evolution. At the beginning of irradiation (Time < 0.62 in Figure 19) the fuel maximum temperature increases as the linear power in the pellet. During this first stage we can see a reduction of the pellet-to-cladding gap which is due to the differential thermal expansion between the pellet and the cladding, and to the fuel relocation induced by the pellet fragmentation as

described in section 5.2.1. In Figure 19, 20% of the gap reduction during the power increase is linked to the fragmentation effect and the other 80% are due to the differential thermal expansion. Just before the end of the power transient, the temperature is high enough (greater than 1800°C) to start the porosity migration process leading to an increasing central hole radius. Consequently, the gap size decreases significantly, like the maximal fuel temperature. This feedback effect between the central hole evolution and the gap size is obtained thanks to the coupling formulation between the mass transfer and the fuel relocation displacement. In Figure 19 we can also see that this second mechanism can lead to a complete closure of the pellet-to-cladding gap, and then consequently to a reduction of 10% of the maximal temperature.

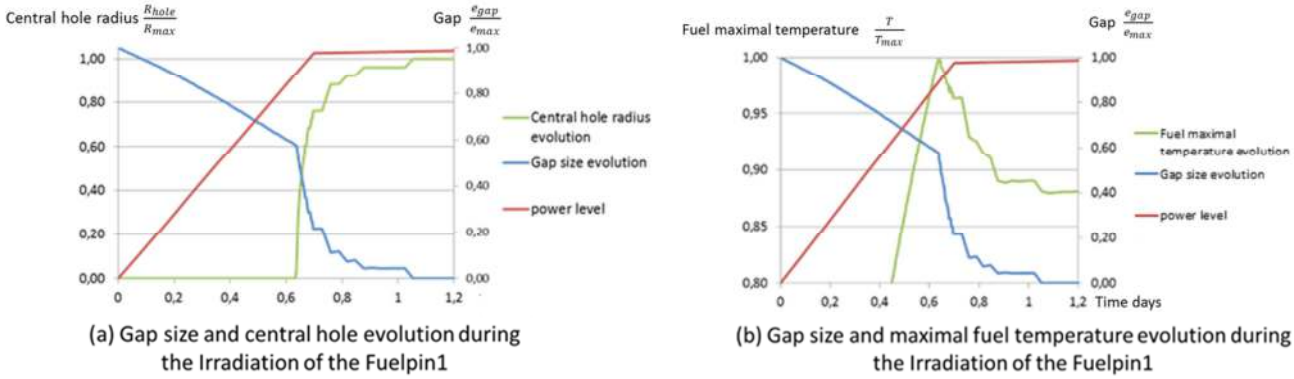

(a) Gap size and central hole evolution during the Irradiation of the Fuelpin1

(b) Gap size and maximal fuel temperature evolution during the Irradiation of the Fuelpin1

Figure 19 – illustration of the coupling between the relocation model, gap size and fuel maximal temperature evolution during irradiation for the Fuelpin1 ($e_{max} = 113\mu m$, $T_{max} = 2266K$ and $R_{max} = 3.45e-4m$)

In Figure 20, sensitivity to the maximum power level is illustrated through the axial distribution of the central hole and the columnar grain zone radii obtained by our new formulation and compared with experiments. The results of the simulation are in good agreement with the experiments for different axial levels considered along the pin, in particular with regard to the dependence to the fuel thermal regime of these two radii. That proves that our new model and coupling formulation allow to properly represent the effect of the thermal regime on the evolution of the central hole and the restructuring zone size.

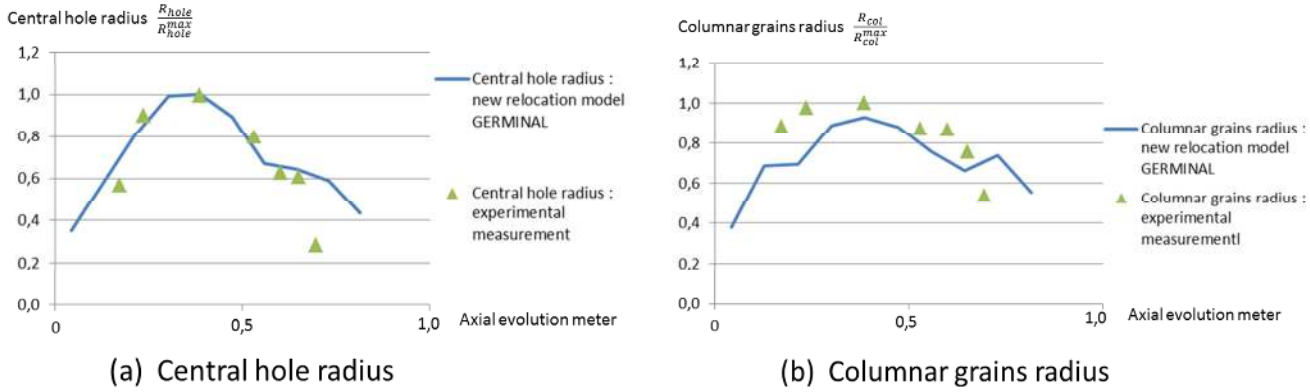

(a) Central hole radius

(b) Columnar grains radius

Figure 20 – Comparison of columnar grains radius and central hole radius obtained with the Fuelpin2 on all axial slices between GERMINAL with new relocation model and experimental results ($R_{hole}^{max} = 6e-4m$ and $R_{col}^{max} = 1.79e-3m$).

As illustrated in Figure 21 with the comparison measurement-simulation, the results obtained with the new relocation model are very satisfactory for both types of geometry tested (full and annular pellets). Compared to the previous relocation model of GERMINAL, we can also observe a significant improvement of the simulation results, especially for the columnar grain zone

radius, for these four pins. These good results and improvements can be clearly attributed to a more physical formulation where the effect of temperature, mass-transfer and geometry are rigorously taken into account in the constitutive equation of the new relocation model.

Nevertheless, some improvements are still needed to precisely model intermediate power levels under which the evaporation-condensation restructuration process is not observed in experiments. Indeed, we can see that the radii of the columnar grain zone and the central hole are over estimated at bottom and top of the fuel pin where fuel temperature is lower due to power profile (see Figure 20 and small radii in Figure 21). This problem seems to be linked to an over estimation of the fuel temperature in these zones which can be the result of an over estimation of the pellet-to-cladding gap or the result of the uncertainties associated to the thermal properties of irradiated (U,Pu)O_2 fuel. Regarding the pellet-to-cladding gap different aspects could be investigated such as:

- To consider fuel temperature variation between the mid pellet plane and the inter-pellet plane in order to compare it with experimental results for which the axial location in the pellet is unknown (it means to introduce the hourglass shape effect neglected because of its low impact on the mid pellet plane temperature).
- Another pellet-to-cladding gap reduction mechanism such as gaseous swelling.

Moreover in order to reduce uncertainties the assumption regarding the migration velocity of the filling porosity could be reconsidered with a detailed modelling of the evaporation-condensation process around cracks.

Despite these limitations, the new relocation model proposed allows to obtain significant improvements with a physically based formulation where each parameter can be adjusted with a separate effect computation.

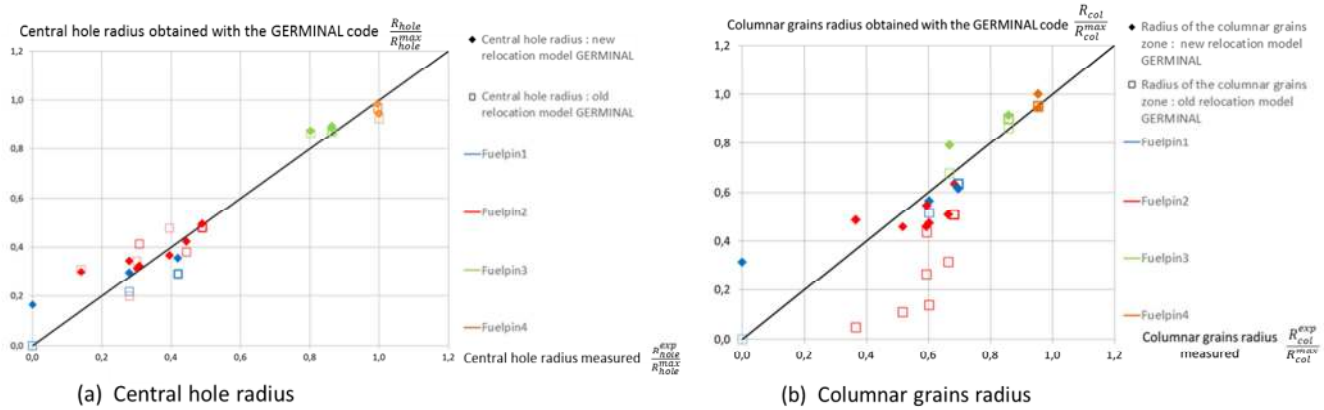

Figure 21 – Comparison of columnar grains radius and central hole radius between GERMINAL, GERMINAL with the new relocation model and experimental measurements ($R_{hole}^{max} = 1.215e-3m$; $R_{col}^{max} = 2.62e-3m$).

6. CONCLUSIONS AND PERSPECTIVES

Some current "1.5D" SFR fuel performance codes have a so-called relocation model to account for phenomena linked to the pellet-to-cladding gap closure. Indeed, the simulation of the pellet-to-cladding gap size is an issue of primary importance to obtain a good estimation of the evolution of the fuel temperature. These models are however empirical and cannot provide a predictive assessment regarding the sensitivity to geometrical and material parameters. In this paper we have proposed a physically based model enabling to simulate the contribution of phenomena responsible of the pellet-to-cladding gap closure. Two main phenomena occurring at the beginning of irradiation have been identified thanks to experimental observations. The first one, quite well known in the literature, is related to the pellet fragmentation and the second one, an original proposition of this work, is related to the mass transfer induced by the fuel restructuration.

These mechanisms have been implemented and validated in a 3D model realized thanks to a one-way coupling process between the 1.5D code GERMINAL and the 3D prototype application LICOS. 3D simulations have been compared to experimental results for full and annular pellet geometries. Results showed that the mass transfer phenomenon is required to obtain columnar grains zone radii in good agreement with experimental measurements. A 1D coupling formulation has then been proposed between porosity migration and central hole formation in order to properly model the mass transfer process. Hence a new relocation model taking account of the fuel fragmentation and the mass transfer has been implemented. A homogeneous relocation strain, used in the mechanical model, is obtained. The fragmentation contribution is obtained thanks to an analytical formulation based on the difference of displacement with an unfragmented pellet. Both full and annular pellet cases have been considered. The mass transfer contribution is obtained thanks to the volume expansion in the restructuring zone induced by the filling porosity migration. Comparisons have been performed between new numerical results and post irradiation measurements of central hole and restructured zone radii. New results obtained with four experimental irradiations of the GERMINAL's validation data base are encouraging. They are in good agreement with experimental results and significant improvements can be expected compared to the previous empirical model. Some limitations remain regarding the relocation process for lower power level, when no central hole is observed, or after the pellet-to-cladding gap closure. Then, in order to extend the validity and the precision of our approach some prospects have been proposed to go further in the physical description of the pellet-to-cladding gap closure phenomenon taking into account for example the hourglass shape effect, the impact of gaseous swelling or a detailed description of the evaporation-condensation process around cracks.

7. ACKNOWLEDGEMENTS

The authors would like to thank Marc Lainet and Renaud Masson for their help in this work and the fruitful discussions regarding modelling and validation in fuel performance codes.

8. REFERENCES

[1] M. Lainet, B. Michel, J.-C. Dumas, M. Pelletier, and I. Ramière, 'GERMINAL, a fuel performance code of the PLEIADES platform to simulate the in-pile behaviour of mixed oxide fuel pins for sodium-cooled fast reactors', Journal of Nuclear Materials, vol. 516, pp. 30–53, Apr. 2019.

[2] A. Boldyrev, S. Yu. Chernov, A. P. Dolgodvorov, V. D. Ozrin, and V. I. Yarasov "BERKUT – Best estimate code for modelling of Fast Reactor Fuel Rod Behaviour under Normal and Accidental Conditions." International Conference on Fast Reactors and Related Fuel Cycles: Next Generation Nuclear Systems for Sustainable Development (FR17), PAPER 363 (june 27, 2017)

[3] D. P. Veprev, A.V. Boldyrev, S.Yu. Chernov, and N. A. Mosunova. "Development and Validation of the BERKUT Fuel Rod Module of the EUCLID/V1 Integrated Computer Code." Annals of Nuclear Energy 113 (March 2018): 237–45.

[4] M. S. Veshchunov, A.V. Boldyrev, A.V. Kuznetsov, V. D. Ozrin, M. S. Seryi, V. E. Shestak, V. I. Tarasov, et al. "Development of the Advanced Mechanistic Fuel Performance and Safety Code Using the Multi-Scale Approach." Nuclear Engineering and Design 295 (Decembre 2015): 116-126

[5] T. Ozawa, and T. Abe. "Development and Verifications of Fast Reactor Fuel Design Code CEPTAR." Nuclear Technology 156, no. 1 (October 2006): 39–55.

[6] A. Karahan. "Modelling of Thermo-Mechanical and Irradiation Behavior of Metallic and Oxide Fuels for Sodium Fast Reactors." Thesis, Massachusetts Institute of Technology, 2009

[7] A. Karahan, and J. Buongiorno "Modeling of Thermo-Mechanical and Irradiation Behavior of Mixed Oxide Fuel for Sodium Fast Reactors." Journal of Nuclear Materials 396, no. 2–3 (January 2010): 272–82.

[8] J. R. Matthews, R. F. Cameron, P. E. Coleman, and R. Thetford "The Application of the TRAFIC Code to Fast Reactor Fuel Transients." Science and Technology of Fast Reactor Safety. Vol. 2, 1987.

[9] F. Gao, Q. Chen, L. Wang "The development of a computer code for predicting fast reactor oxide fuel element thermal and mechanical behaviour (FIBER-Oxide)." International Conference on Fast Reactors and Related Fuel Cycles: Next Generation Nuclear Systems for Sustainable Development (FR17), PAPER217 (june 29, 2017)

[10] C. Fiorina, A. Pautz and K. Mikityuk. "Creation of an OPENFOAM fuel performance class based on FRED and integration inti the GEN-FOAM multi-physics code." Proceedings of International Conference on Nuclear Engineering ICONE 2018 July 22-26, 2018, London, UK.

[11] V. Z Jankus, and R. W. Weeks "LIFE-II - A Computer Analysis of Fast-Reactor Fuel-Element Behavior as a Function of Reactor Operating History." Nuclear Engineering and Design 18, no. 1 (January 1, 1972): 83–96.

[12] T. Helfer, S. Bejaoui, B. Michel, "LICOS, a fuel performance code for innovative fuel elements or experimental devices design",Nuclear Engineering and Design, Volume 294, Pages 117-136, 2015.

[13] B. Michel, C. Nonon, J. Sercombe, F. Michel, and V. Marelle, 'Simulation of Pellet-Cladding Interaction with the PLEIADES Fuel Performance Software Environment', Nuclear Technology, vol. 182, no. 2, pp. 124–137, May 2013.

[14] V. Marelle "Validation of PLEIADES/ALCYONE 2.0 fuel performance code", Water Reactor Fuel Performance Meeting/TopFuel Conference, Jeju Island, Korea (2017).

[15] C. Prunier, H. Baily. "Le combustible nucléaire des réacteurs à eau sous pression et des réacteurs à neutrons rapides." Denise Ménessier, Eyrolles, 1996.

[16] P. F. Sens "The Kinetics of Pore Movement in UO2 Fuel Rods." Journal of Nuclear Materials 43, no. 3 (June 1, 1972): 293–307.

[17] H. Hoffmann "Crack Formation, Crack Healing and Porosity Redistribution during Irradiation of UO2 and (U, Pu) O2." Journal of Nuclear Materials 54, no. 1 (November 1, 1974): 9–23.

[18] DEN Monographs "nuclear fuels: Nuclear Energy Direction" p92 - http://www.materials.cea.fr/PDF/MonographiesDEN/Lescombustiblesnucleaires-CEA-fr.pdf.

[19] Y. Guerin. “2.21 - Fuel Performance of Fast Spectrum Oxide Fuel.” In *Comprehensive Nuclear Materials*, edited by Rudy J. M. Konings, 547–78. Oxford: Elsevier, 2012.

[20] M. Oguma, ‘Cracking and relocation behavior of nuclear fuel pellets during rise to power’, Nuclear Engineering and Design, vol. 76, no. 1, pp. 35–45, Oct. 1983.

[21] L. A. Walton and J. E. Matheson, ‘FUMAC—A New Model for Light Water Reactor Fuel Relocation and Pellet-Cladding Interaction’, Nuclear Technology, May 2017.

[22] L. A. Walton and D. L. Husser. ‘Fuel pellet fracture and relocation’. In J. H. Gittus, editor, Water Reactor Fuel Element Performance Computer Modelling. Applied Science Publishers, London, UK, 1984.

[23] G.-P. Mezzi, F. Caligara, and H. Blank, ‘Thermoelastic stresses in pellet fragments and conditions for fragments formation’, Nuclear Engineering and Design, vol. 73, no. 1, pp. 83–93, Oct. 1982.

[24] V. Guicheret-Retel, F. Trivaudey, M. L. Boubakar, and P. Thevenin, ‘Elastic and viscoplastic pellets fragmentation modeling using an axisymmetrical 1D finite element code’, Nuclear Engineering and Design, vol. 232, no. 3, pp. 249–262, Aug. 2004.

[25] L. Van Brutzel, R. Dingreville, and T.J. Bartel. “Nuclear fuel deformation phenomena”. State of-the-Art Report on Multi-scale Modelling of Nuclear Fuels. OECD/NEA Working Party on Multi-scale Modelling of Fuels and Structural Materials for Nuclear Systems, 59, 2015

[26] David Carpenter. Comparison of Pellet-Cladding Mechanical Interaction for Zircaloy and Silicon Carbide Clad Fuel Rods in Pressurized Water Reactors. MIT Department of Nuclear Engineering. December 11, 2006.

[27] A.S. Bain “Cracking and bulk movement in irradiated uranium oxide fuel elements” Trans Am Nucl Soc 1963.

[28] F. Tavangarian “Crack Self-Healing in SiC/Spinel Nanocomposite.” LSU Doctoral Dissertations, January 1, 2014. https://digitalcommons.lsu.edu/gradschool_dissertations/1980.

[29] J. T. A. Roberts, and B. J. Wrona “Crack Healing in UO2.” Journal of the American Ceramic Society 56, no. 6 (June 1, 1973): 297–99.

[30] D. G. Krige “A statistical approach to some mine valuations and allied problems at the Witwatersrand”, Master's thesis of the University of Witwatersrand, 1951.

[31] B. Michel , M. Temmar, M. Lainet, I. Ramière, M. Pelletier, JC. Dumas. 3D simulation in the PLEIADES software environment for sodium fast reactor fuel pin behavior under irradiation, Fast Reactor FR17 Yekaterinburg Russie, June 26-29,2017

[32] R. C. Reid, J. M Prausnitz, and B. E. Polin The Properties of Gases and Liquids. New York: McGraw-Hill, 1987.

[33] J. O. Hirschfelder, C. F. Curtiss and R. B. Bird. “Molecular Theory of Gases and Liquids.” Corrected Printing with Notes Added. Wiley, 1964.

[34] S. Ghosh, S. Dobbie, J. Marsham, and P. R. Jonas. “On the Importance of the Diffusional Uptake of Water Vapour for the Development and Radiative Properties of High Altitude Clouds: A Large Eddy Model Sensitivity Study.” Quarterly Journal of the Royal Meteorological Society 133, no. 628 (October 1, 2007): 1731–41.

[35] P. D. Neufeld, A. R. Janzen, and R. A. Aziz “Empirical Equations to Calculate 16 of the Transport Collision Integrals Ω(l, s) for the Lennard-Jones (12–6) Potential.” The Journal of Chemical Physics 57, no. 3 (August 1, 1972): 1100–1102.

[36] N. I. Muskhelishvili “Some basic problems of the mathematical theory of elasticity”, 4ème edition, P. Noordhoff, Groningen-The Netherlands (1963).

[37] J.Sercombe, R.Masson, and T.Helfer. “Stress Concentration during Pellet Cladding Interaction: Comparison of Closed-Form Solutions with 2D(r,θ) Finite Element Simulations.” Nuclear Engineering and Design 260 (July 2013): 175–87.

[38] A. H. England. “Complex Variable Methods in Elasticity”, Dover Publications, Mineola, New York (2003).

[39] Lawrence C. Evans. “Partial Differential Equations, Graduate Studies in Mathematics.” Vol. 19, American Mathematical Society (1998).

9. APPENDIX 1: STRESS TENSOR EXPRESSION FOR A FULL AND ANNULAR PELLET IN THE CASE OF AN UN-FRAGMENTED PELLET

Un-fragmented pellet

- Full pellet

$$\sigma_{rr}^{full-axi}(r) = -\frac{2G}{1-\nu}\left[\frac{\varepsilon_1^{full}}{2} + \frac{\varepsilon_3^{full}}{4}r^2\right] + \frac{2G}{1-2\nu}a \quad \text{(A- 1)}$$

$$\sigma_{\theta\theta}^{full-axi}(r) = -\frac{2G}{1-\nu}\left[\frac{\varepsilon_1^{full}}{2} + \frac{3\varepsilon_3^{full}}{4}r^2\right] + \frac{2G}{1-2\nu}a$$

- Annular pellet

$$\sigma_{rr}^{an-axi}(r) = -\frac{2G}{1-\nu}\left[\frac{\varepsilon_1^{an}}{2}\left(1-\frac{R_i^2}{r^2}\right) + \frac{\varepsilon_2^{an}}{2}\left(\ln(r) - \frac{R_i^2}{r^2}\ln(R_i) - \frac{1}{2} + \frac{R_i^2}{2r^2}\right) + \frac{\varepsilon_3^{an}}{4}\left(r^2 - \frac{R_i^4}{r^2}\right)\right] + \frac{2G}{1-2\nu}c - 2G\frac{b}{r^2} \quad \text{(A- 2)}$$

$$\sigma_{\theta\theta}^{an-axi}(r) = -\frac{2G}{1-\nu}\left[\frac{\varepsilon_1^{an}}{2}\left(1+\frac{R_i^2}{r^2}\right) + \frac{\varepsilon_2^{an}}{2}\left(\ln(r) + \frac{R_i^2}{r^2}\ln(R_i) + \frac{1}{2} - \frac{R_i^2}{2r^2}\right) + \frac{\varepsilon_3^{an}}{4}\left(3r^2 + \frac{R_i^4}{r^2}\right)\right] + \frac{2G}{1-2\nu}c + 2G\frac{b}{r^2}$$

With boundary conditions we deduce the expression of constants for the un-fragmented pellet as follows:

$$\sigma_{rr}^{full-axi}(R_e) = 0 \;\rightarrow\; a = \frac{1-2\nu}{2(1-\nu)}\left(\varepsilon_1^{full} + \frac{\varepsilon_3^{full}}{2}R_e^2\right) \quad \text{(A- 3)}$$

$$\begin{cases}\sigma_{rr}^{an-axi}(R_e) = 0\\ \sigma_{rr}^{an-axi}(R_i) = 0\end{cases} \rightarrow \begin{matrix} c = \frac{1-2\nu}{2(1-\nu)}\left[\varepsilon_1^{an} + \frac{\varepsilon_2^{an}\left(\ln(R_i)R_i^2 - \ln(R_e)R_e^2\right)}{R_i^2 - R_e^2} - \frac{\varepsilon_2^{an}}{2} + \frac{\varepsilon_3^{an}}{2}\left(R_i^2 + R_e^2\right)\right] \\ b = \frac{1}{2(1-\nu)}\left[\varepsilon_1^{an}R_i^2 + \frac{\varepsilon_2^{an}\left(\ln(R_i)R_i^4 - \ln(R_e)R_e^2R_i^2\right)}{R_i^2 - R_e^2} - \frac{\varepsilon_2^{an}}{2}R_i^2 + \frac{\varepsilon_3^{an}}{2}R_i^2\left(R_i^2 + R_e^2\right)\right]\end{matrix} \quad \text{(A- 4)}$$

We can deduce the following expression of displacement field in function of the temperature for a full and annular pellet:

$$u_r^{full-axi}(r) = \frac{\alpha}{r}\left[\frac{1}{(1-\nu)}\int_0^r Trdr + \frac{(1-2\nu)r^2}{(1-\nu)R_e^2}\int_0^{R_e} Trdr\right] \quad \text{(A- 5)}$$

$$u_r^{an-axi}(r) = \frac{\alpha}{r}\left[\frac{1}{(1-\nu)}\int_{R_i}^r Trdr + \frac{(1-2\nu)r^2 + R_i^2}{(1-\nu)\left(R_e^2 - R_i^2\right)}\int_{R_i}^{R_e} Trdr\right] \quad \text{(A- 6)}$$

10. APPENDIX 2: MUSKHELISHVILI METHOD: DISPLACEMENT FIELD SOLUTION OF THE MECHANICAL EQUILIBRIUM EQUATION ON A 2D CYLINDRICAL SECTOR SUBMITTED TO A THERMAL GRADIENT

This approach consists in describing the displacement field as a function of two potentials $(\Omega(z), w(z))$ of the complex variable $z = x + iy$. If no body forces are applied to this solid, the two components of the displacement field, denoted by $u_x(x,y)$ and $u_y(x,y)$ in cartesian coordinates, can be expressed as follows ([36] and [37]):

$$u_x + iu_y = D(z) = \frac{1}{2G}\left[(3-4\nu)\Omega(z) - z\overline{\Omega'(z)} - \overline{w(z)}\right] \quad \text{(A- 7)}$$

If the derivatives of the two complex potentials are holomorphic functions of the complex variable $f'(z_0) = \lim_{z->z_0} \frac{f(z)-f(z_0)}{z-z_0}$, the stress field satisfies the equilibrium equations. An additional term to taking account of the isotropic stress free strain ε^{th} (see equations (25), (26) and (27)) is then introduced.

The solution for a full and annular pellet is defined as follows: ([36] see indication pp165-170 and [38]

$$D_{full}(z) = \frac{1}{2G}\left[(3-4\nu)\Omega_{full}(z) - z\overline{\Omega_{full}{}'(z)} - \overline{w_{full}(z)}\right] + \widetilde{D_{full}}(z) \quad \text{(A- 8)}$$
$$+\left(\frac{1}{1-\nu)}\right)\frac{1}{\bar{z}}\left(\int_0^{\sqrt{z\bar{z}}} \varepsilon_3^{full} t^3 dt\right)$$

such as : $\widetilde{D_{full}}(z) = \varepsilon_1^{full} z$

$$D_{an}(z) = \frac{1}{2G}\left[(3-4\nu)\Omega_{an}(z) - z\overline{\Omega_{an}{}'(z)} - \overline{w_{an}(z)}\right] + \widetilde{D_{an}}(z) \quad \text{(A- 9)}$$
$$+\frac{1}{\bar{z}}\left(\left(\frac{1}{1-\nu}\right)\int_{R_i}^{\sqrt{z\bar{z}}} \varepsilon_3^{an} t^3 dt + d\right)$$

such as : $\widetilde{D_{an}}(z) = \varepsilon_1^{an} z + \varepsilon_2^{an}(z\ln(z) - z)$

The displacement field respects the equilibrium equation by construction; $\widetilde{D_{full}}(z)$ and $\widetilde{D_{an}}(z)$ refer respectively to the solution obtained by considering only the harmonic distribution of the isotropic stress free strain $\bar{\bar{\varepsilon}}^{th}$ ([36] see indication pp 167) for a full and annular pellet (see equations (25), (26) and (27)). The other part of the solution is obtained by considering the non-harmonic distribution [38] (see pp 21-31).

Considering the different assumptions made, the two complex potentials chosen in [37] are:

$$\begin{cases} \Omega_{full}(z) = \gamma^{full}(G,\nu)\varepsilon_3^{full} z^3 + A\ln\left(\frac{z}{r_0}\right) \\ w_{full}(z) = \beta^{full}(G,\nu)\varepsilon_3^{full} z^3 - A\ln\left(\frac{z}{r_0}\right) \end{cases} \quad \text{(A- 10)}$$

γ^{full}, β^{full} and r_0 are parameters to be defined with the boundary conditions

For the annular pellet we chose the same expression for the two potentials than the full pellet, but r_0 is replaced by R_i and the constants are different:

$$\begin{cases} \Omega_{an}(z) = \gamma^{an}(G,\nu)\varepsilon_3^{an} z^3 + B\ln\left(\frac{z}{R_i}\right) \\ w_{an}(z) = \beta^{an}(G,\nu)\varepsilon_3^{an} z^3 - B\ln\left(\frac{z}{R_i}\right) \end{cases} \quad \text{(A- 11)}$$

γ^{an} and β^{an} are parameters to be defined with the boundary conditions

The radial component of the displacement field for a full and annular pellet can be deduced from Cartesian solution as follow:

$$u_x^{full-frag} + iu_y^{full-frag} = D_{full}(z) = \frac{1}{2G}\left[(3(z^2-\bar{z}^2)z - 4\nu z^3)\gamma^{full}(G,\nu)\varepsilon_3^{full} - \beta^{full}(G,\nu)\varepsilon_3^{full}\bar{z}^3\right] + \varepsilon_1^{full}z + \left(\frac{1}{1-\nu}\right)\frac{1}{\bar{z}}\left(\int_0^{\sqrt{z\bar{z}}}\varepsilon_3^{full}t^3dt\right) + \frac{A}{2G}\left[(3-4\nu)\ln\left(\frac{z}{r_0}\right) - \frac{z}{\bar{z}} + \ln\left(\frac{\bar{z}}{r_0}\right)\right] \quad \text{(A- 12)}$$

$$u_x^{an-frag} + iu_y^{an-frag} = D_{an}(z) = \frac{1}{2G}\left[(3(z^2-\bar{z}^2)z - 4\nu z^3)\gamma^{an}(G,\nu)\varepsilon_3^{an} - \beta^{full}(G,\nu)\varepsilon_3^{an}\bar{z}^3\right] + \varepsilon_1^{an}z + \varepsilon_2^{an}(z\ln(z) - z) + \frac{1}{\bar{z}}\left(\left(\frac{1}{1-\nu}\right)\int_{R_i}^{\sqrt{z\bar{z}}}\varepsilon_3^{an}t^3dt + d\right) + \frac{B}{2G}\left[(3-4\nu)\ln\left(\frac{z}{R_i}\right) - \frac{z}{\bar{z}} + \ln\left(\frac{\bar{z}}{R_i}\right)\right] \quad \text{(A- 13)}$$

by using Moivre formula:

$$z^k = r^k e^{ik\theta} = r^k(\cos(k\theta) + i\sin(k\theta))$$
$$\bar{z}^k = r^k e^{-ik\theta} = r^k(\cos(k\theta) - i\sin(k\theta)) \quad \text{(A- 14)}$$

The Cartesian displacement field becomes:

$$u_x^{full-frag} + iu_y^{full-frag} = \frac{1}{2G}\left[(6(i\sin(2\theta)\cos(\theta) - \sin(2\theta)\sin(\theta)) - 4\nu(\cos(3\theta) + i\sin(3\theta))\gamma^{full}(G,\nu)\varepsilon_3^{full} - \beta^{full}(G,\nu)\varepsilon_3^{full}(\cos(3\theta) - i\sin(3\theta))\right]r^3 + \varepsilon_1^{full}r(\cos(\theta) + i\sin(\theta)) + \left(\frac{1}{1-\nu}\right)\frac{(\cos(\theta)+i\sin(\theta))}{r}\left(\int_0^r \varepsilon_3^{full}t^3dt\right) + \frac{A}{2G}\left[3\ln(r) + 3i\theta + \ln(r) - i\theta - (\cos(2\theta) + i\sin(2\theta)) + (4-4\nu)\ln\left(\frac{1}{r_0}\right) - 4\nu\ln(r) - 4i\theta\right] \quad \text{(A- 15)}$$

$$u_x^{an-frag} + iu_y^{an-frag} = \frac{1}{2G}\left[(6(i\sin(2\theta)\cos(\theta) - \sin(2\theta)\sin(\theta)) - 4\nu(\cos(3\theta) + i\sin(3\theta))\gamma^{an}(G,\nu)\varepsilon_3^{an} - \beta^{an}(G,\nu)\varepsilon_3^{an}(\cos(3\theta) - i\sin(3\theta))\right]r^3 + \varepsilon_1^{an}r(\cos(\theta) + i\sin(\theta)) + \varepsilon_2^{an}r(\cos(\theta)\ln(r) + i\sin(\theta)\ln(r) + \cos(\theta)i\theta - \sin(\theta)\theta - \cos(\theta) - i\sin(\theta)) + \frac{(\cos(\theta)+i\sin(\theta))}{r}\left(\left(\frac{1}{1-\nu}\right)\int_{R_i}^r \varepsilon_3^{an}t^3dt + d\right) + \frac{B}{2G}\left[3\ln(r) + 3i\theta + \ln(r) - i\theta - (\cos(2\theta) + i\sin(2\theta)) + (4-4\nu)\ln\left(\frac{1}{R_i}\right) - 4\nu\ln(r) - 4i\theta\right] \quad \text{(A- 16)}$$

By projecting the Cartesian displacement fields in the cylindrical system:

$$u_r\,\overrightarrow{e_r} = u_x\cos\theta\overrightarrow{e_x} + u_y\sin\theta\overrightarrow{e_y} \qquad \text{(A- 17)}$$

where, $u_x = \mathrm{Re}\big(D(z)\big)$ and $u_y = \mathrm{Im}\big(D(z)\big)$

we can deduce the expression of the displacement field radial component for a full and annular pellet:

$$u_r^{full-frag}(r,\theta) = \frac{1}{2G}\big[-4\nu(\cos(3\theta)\cos(\theta)+\sin(3\theta)\sin(\theta))\gamma^{full}(G,\nu)\varepsilon_3^{full} - \beta^{full}(G,\nu)\varepsilon_3^{full}(\cos(3\theta)\cos(\theta) - \sin(3\theta)\sin(\theta))\big]r^3 + \varepsilon_1^{full}r(\cos(\theta)^2+\sin(\theta)^2) + \left(\frac{1}{1-\nu)}\right)\frac{(\cos(\theta)^2+\sin(\theta)^2)}{r}\left(\int_0^r \varepsilon_3^{full}t^3dt\right) + \frac{A}{2G}\left[(4-4\nu)\ln\left(\frac{r}{r_0}\right)\cos(\theta) + (2-4\nu)\sin(\theta)\theta - (\cos(2\theta)\cos(\theta)+\sin(2\theta)\sin(\theta))\right] \qquad \text{(A- 18)}$$

$$u_r^{an-frag}(r,\theta) = \frac{1}{2G}[-4\nu(\cos(3\theta)\cos(\theta)+\sin(3\theta)\sin(\theta))\gamma^{an}(G,\nu)\varepsilon_3^{an} - \beta^{an}(G,\nu)\varepsilon_3^{an}(\cos(3\theta)\cos(\theta) - \sin(3\theta)\sin(\theta))]r^3 + \varepsilon_1^{an}r(\cos(\theta)^2+\sin(\theta)^2) + \varepsilon_2^{an}r[(\cos(\theta)^2+\sin(\theta)^2)\ln(r) + (\cos(\theta)\sin(\theta) - \sin(\theta)\cos(\theta))\theta - (\cos(\theta)^2+\sin(\theta)^2)] + \frac{(\cos(\theta)^2+\sin(\theta)^2)}{r}\left(\left(\frac{1}{1-\nu)}\right)\int_{R_i}^r \varepsilon_3^{an}t^3dt + d\right) + \frac{B}{2G}\left[(4-4\nu)\ln\left(\frac{r}{R_i}\right)\cos(\theta) + (2-4\nu)\sin(\theta)\theta - (\cos(2\theta)\cos(\theta)+\sin(2\theta)\sin(\theta))\right] \qquad \text{(A- 19)}$$

by using the following expression:

$$\begin{aligned}&\cos(\theta)^2+\sin(\theta)^2 = 1\\ &\cos(p-q) = \cos(p)\cos(q)+\sin(p)\sin(q)\\ &\cos(p)+\cos(q) = 2\cos\left(\frac{p+q}{2}\right)\cos\left(\frac{p-q}{2}\right)\\ &\cos(p)-\cos(q) = -2\sin\left(\frac{p+q}{2}\right)\sin\left(\frac{p-q}{2}\right)\end{aligned} \qquad \text{(A- 20)}$$

we can finally obtain the radial displacement field component for a full and annular pellet:

$$u_r^{full-frag}(r,\theta) = \frac{1}{2G}\big[-4\nu\cos(2\theta)\,\gamma^{full}(G,\nu)\varepsilon_3^{full} - \beta^{full}(G,\nu)\varepsilon_3^{full}\cos(4\theta)\big]r^3 + \varepsilon_1^{full}r + \left(\frac{1}{1-\nu)}\right)\frac{1}{r}\left(\int_0^r \varepsilon_3^{full}t^3dt\right) + \frac{A}{2G}\left[(4-4\nu)\cos(\theta)\ln\left(\frac{r}{r_0}\right) + (2-4\nu)\theta\sin(\theta) - \cos(\theta)\right] \qquad \text{(A- 21)}$$

$$u_r^{an-frag}(r,\theta) = \frac{1}{2G}[-4\nu\cos(2\theta)\gamma^{an}(G,\nu)\varepsilon_3^{an} - \beta^{an}(G,\nu)\varepsilon_3^{an}\cos(4\theta)]r^3 + \varepsilon_1^{an}r + \varepsilon_2^{an}r[\ln(r) - 1] + \frac{1}{r}\left(\left(\frac{1}{1-\nu)}\right)\int_{R_i}^r \varepsilon_3^{an}t^3dt + d\right) + \frac{B}{2G}\left[(4-4\nu)\cos(\theta)\ln\left(\frac{r}{R_i}\right) + (2-4\nu)\theta\sin(\theta) - \cos(\theta)\right] \qquad \text{(A- 22)}$$

The parameters γ^{full}, γ^{an} , β^{full}, β^{an} , as well as A, B , and d are calculated in Appendix 3.

11. APPENDIX 3: STRESS TENSOR EXPRESSION FOR A FULL AND ANNULAR PELLET IN THE CASE OF A FRAGMENTED PELLET

Fragmented pellet

- Full pellet

$$\sigma_{r\theta}^{full-frag}(r,\theta) = 3\varepsilon_3^{full} r^2 \left[\gamma^{full}(G,\nu)\sin(2\theta) + \beta^{full}(G,\nu)\sin(4\theta)\right]$$

$$\sigma_{\theta\theta}^{full-frag}(r,\theta) = 3\varepsilon_3^{full} r^2 \left[-\frac{1}{1-\nu}\frac{2G}{4} + 4\gamma^{full}(G,\nu)\cos(2\theta) + \beta^{full}(G,\nu)\cos(4\theta)\right] \quad \text{(A- 23)}$$

$$\sigma_{rr}^{full-frag}(r,\theta) = \varepsilon_3^{full} r^2 \left[-\frac{1}{1-\nu}\frac{2G}{4} - 3\beta^{full}(G,\nu)\cos(4\theta)\right] + \frac{4A\cos(\theta)}{r}$$

Using boundary conditions we deduce the expression of constants for the fragmented full pellet as follows:

$$\begin{cases}\sigma_{r\theta}^{full-frag}(r,\pm\theta_m) = 0 \\ \sigma_{\theta\theta}^{full-frag}(r,\pm\theta_m) = 0\end{cases} \rightarrow \begin{array}{l}\gamma^{full}(G,\nu) = \frac{G}{4}\frac{1}{1-\nu}\frac{1}{\sqrt{2}} \\ \beta^{full}(G,\nu) = -\frac{G}{4}\frac{1}{1-\nu}\end{array}$$

$$\frac{1}{2\theta_m}\int_{-\theta_m}^{\theta_m} \sigma_{rr}^{full-frag}(R_e,\theta)d\theta = 0 \rightarrow A = \frac{\varepsilon_3^{full} R_e^3}{4\sin\left(\frac{\pi}{8}\right)}\left[\frac{2G}{4(1-\nu)}\frac{\pi}{8} + \frac{3\beta^{full}(G,\nu)}{4}\right] \quad \text{(A- 24)}$$

$$\begin{cases}\frac{1}{2\theta_m}\int_{-\theta_m}^{\theta_m} u_r^{full-frag}(r_i,\theta)d\theta = 0 \\ r_i \ll R_e\end{cases} \rightarrow \ln(r_0) = \frac{(2-4\nu)\left(\sin\left(\frac{\pi}{8}\right)-\frac{\pi}{8}\cos\left(\frac{\pi}{8}\right)\right)-\sin\left(\frac{\pi}{8}\right)}{(4-4\nu)\sin\left(\frac{\pi}{8}\right)} + \ln(r_i)$$

- Annular pellet

$$\sigma_{r\theta}^{an-frag}(r,\theta) = 3\varepsilon_3^{an} r^2 [\gamma^{an}(G,\nu)\sin(2\theta) + \beta^{an}(G,\nu)\sin(4\theta)]$$

$$\sigma_{\theta\theta}^{an-frag}(r,\theta) = 3\varepsilon_3^{an} r^2 \left[-\frac{1}{1-\nu}\frac{2G}{4}\left(1+\frac{R_i^4}{3r^4}\right) + 4\gamma^{an}(G,\nu)\cos(2\theta) + \beta^{an}(G,\nu)\cos(4\theta)\right] + 2G\frac{d}{r^2} \quad \text{(A- 25)}$$

$$\sigma_{rr}^{an-frag}(r,\theta) = \varepsilon_3^{an} r^2 \left[-\frac{1}{1-\nu}\frac{2G}{4}\left(1-\frac{R_i^4}{r^4}\right) - 3\beta^{an}(G,\nu)\cos(4\theta)\right] - 2G\frac{d}{r^2} + \frac{4B\cos(\theta)}{r}$$

Using boundary conditions we deduce the expression of constants for the fragmented annular pellet as follows:

$$\begin{cases} \sigma_{r\theta}^{an-frag}(r,\pm\theta_m)=0 \\ \frac{1}{(R_e-R_i)}\int_{R_i}^{R_e}\sigma_{\theta\theta}^{an-frag}(r,\pm\theta_m)=0 \end{cases} \rightarrow \begin{aligned} \gamma^{an}(G,\nu) &= \frac{G}{4}\frac{1}{1-\nu}\frac{\pi}{\sqrt{2}}\frac{R_e^3}{(R_e^3-R_i^3)}\left[\frac{1-\frac{R_i^3}{Re^3}}{(R_e-R_i)}-\frac{1-\frac{R_i^4}{Re^4}}{(R_e+R_i)}-\frac{R_i^3}{R_e^4}\right]\frac{(R_e^2-R_i^2)}{\pi(R_e+R_i)-3(R_e-R_i)} \\ \beta^{an}(G,\nu) &= -\frac{G}{4}\frac{\pi}{1-\nu}\frac{R_e^3}{(R_e^3-R_i^3)}\left[\frac{1-\frac{R_i^3}{Re^3}}{(R_e-R_i)}-\frac{1-\frac{R_i^4}{Re^4}}{(R_e+R_i)}-\frac{R_i^3}{R_e^4}\right]\frac{(R_e^2-R_i^2)}{\pi(R_e+R_i)-3(R_e-R_i)} \end{aligned} \quad \text{(A- 26)}$$

$$\begin{cases} \frac{1}{2\theta_m}\int_{-\theta_m}^{\theta_m}\sigma_{rr}^{an-frag}(R_e,\theta)d\theta=0 \\ \frac{1}{2\theta_m}\int_{-\theta_m}^{\theta_m}\sigma_{rr}^{an-frag}(R_i,\theta)d\theta=0 \end{cases} \rightarrow \begin{aligned} d &= \varepsilon_3^{an}\left[\frac{3\beta^{an}(G,\nu)(R_e^3-R_i^3)}{G\pi}+\frac{(R_e^4-R_i^4)}{4(1-\nu)R_e}\right]\frac{R_eR_i}{(R_e+R_i)} \\ B &= \frac{\varepsilon_3^{an}}{4\sin\left(\frac{\pi}{8}\right)}\left[\frac{3\beta^{an}(G,\nu)}{4}+\frac{2G\pi}{4(1-\nu)8}\right]\frac{(R_e^4-R_i^4)}{(R_e-R_i)} \end{aligned}$$

12. APPENDIX 4 : THE STEP OF CALCULATION TO ESTIMATE $\Delta\mathbf{u_r}$

Step 1: assessment of Δu_r:

$$\begin{aligned}\Delta u_r^{full}(r,\theta) &= u_r^{full-frag}(r,\theta) - u_r^{full}(r)\\ &= \varepsilon_3^{full}\left[-\frac{1}{2G}\left[4\nu\gamma^{full}(G,\nu)\cos(2\theta)+\beta^{full}(G,\nu)\cos(4\theta)\right]\right]r^3+\varepsilon_1^{full}r+\frac{A}{2G}\left[(4-4\nu)\cos(\theta)\ln\left(\frac{r}{r_0}\right)+\right.\\ &\left.(2-4\nu)\theta\sin(\theta)-\cos(\theta)\right] - \left[\left(\frac{1}{1-\nu)}\right)\frac{1}{r}\left(\int_0^r\left(\varepsilon_1^{full}t\right)dt\ \right)+ar\right]\end{aligned} \quad \text{(A- 27)}$$

$$\begin{aligned}\Delta u_r^{an}(r,\theta) &= u_r^{an-frag}(r,\theta) - u_r^{an}(r)\\ &=\varepsilon_3^{an}\left[-\frac{1}{2G}\left[4\nu\gamma^{an}(G,\nu)\cos(2\theta)+\beta^{an}(G,\nu)\cos(4\theta)\right]\right]r^3+\varepsilon_1^{an}r+\ \varepsilon_2^{an}r(\ln(r)-1)+\frac{d}{r}\\ &+\frac{B}{2G}\left[(4-\ 4\nu)\cos(\theta)\ln\left(\frac{r}{R_i}\right)+(2-4\nu)\theta\sin(\theta)-\cos(\theta)\right] - \left[\left(\frac{1}{1-\nu)}\right)\frac{1}{r}\left(\int_{R_i}^r t(\varepsilon_1^{an}+\varepsilon_2^{an}\ln(t))dt\ \right)+\frac{b}{r}+cr\right]\end{aligned} \quad \text{(A- 28)}$$

Step 2: assessment of the maximum value of Δu_r:

$$\begin{aligned}\Delta u_r^{full}\left(R_e,\frac{\pi}{8}\right) &= \varepsilon_3^{full}\left[-\frac{1}{2G}\left[4\nu\gamma^{full}(G,\nu)\frac{\sqrt{2}}{2}\right]\right]{R_e}^3+\varepsilon_1^{full}R_e+\frac{A}{2G}\left[(4-4\nu)\cos\left(\frac{\pi}{8}\right)\ln\left(\frac{R_e}{r_0}\right)+(2-4\nu)\frac{\pi}{8}\sin\left(\frac{\pi}{8}\right)-\right.\\ &\left.\cos\left(\frac{\pi}{8}\right)\right] - \left[\left(\frac{1}{1-\nu)}\right)\frac{1}{R_e}\left(\int_0^{R_e}t\left(\varepsilon_1^{full}\right)dt\ \right)+aR_e\right]\end{aligned} \quad \text{(A- 29)}$$

$$\begin{aligned}\Delta u_r^{an}\left(R_e,\frac{\pi}{8}\right) &= \varepsilon_3^{an}\left[-\frac{1}{2G}\left[4\nu\gamma^{an}(G,\nu)\frac{\sqrt{2}}{2}\right]\right]{R_e}^3+\varepsilon_1^{an}R_e+\ \varepsilon_2^{an}R_e(\ln(R_e)-1)\ +\frac{d}{R_e}\\ &+\frac{B}{2G}\left[(4-4\nu)\cos\left(\frac{\pi}{8}\right)\ln\left(\frac{R_e}{R_i}\right)+\ (2-4\nu)\frac{\pi}{8}\sin\left(\frac{\pi}{8}\right)-\cos\left(\frac{\pi}{8}\right)\right]\\ &-\left[\left(\frac{1}{1-\nu)}\right)\frac{1}{R_e}\left(\int_{R_i}^{R_e}t(\varepsilon_1^{an}+\varepsilon_2^{an}\ln(t))dt\ \right)+\frac{b}{R_e}+cR_e\right]\end{aligned} \quad \text{(A- 30)}$$

Step 3: substitution of the constant value

Full pellet:

$$\Delta u_r^{full}\left(R_e,\frac{\pi}{8}\right) = -k_{full}\varepsilon_3^{full}R_e^3 \quad \text{(A- 31)}$$

$$k_{full} = \frac{1}{4}\left[1+\left(\frac{1}{\tan\left(\frac{\pi}{8}\right)}-\frac{(2-4\nu)\pi}{8}\right)\left(\frac{\pi-3}{32(1-\nu)}\right)-\left[\ln\left(\frac{R_e}{r_0}\right)\frac{(\pi-3)}{8\tan\left(\frac{\pi}{8}\right)}\right]\right]$$

Annular pellet:

Knowing that $\varepsilon_2^{an} = -2\varepsilon_3^{an}R_i^2$ (see equation (26)), we deduce:

$$\Delta u_r^{an}\left(R_e, \frac{\pi}{8}\right) = -\varepsilon_3^{an}\left[\frac{(1-2\nu)}{4(1-\nu)}R_e^3 + 2\frac{R_i^4 R_e}{R_i^2 - R_e^2}\ln\left(\frac{R_e}{R_i}\right) - 4\nu\gamma^{an}(G,\nu)\frac{\sqrt{2}}{2}\frac{R_e^3}{2G}\right] + \frac{d}{R_e}$$
$$+\frac{B}{2G}\left[(4-4\nu)\cos\left(\frac{\pi}{8}\right)\ln\left(\frac{R_e}{R_i}\right) + (2-4\nu)\frac{\pi}{8}\sin\left(\frac{\pi}{8}\right) - \cos\left(\frac{\pi}{8}\right)\right] \quad \text{(A- 32)}$$

By considering the annular pellet geometry ($R_e^2 \gg R_i^2$), the following assumptions can be made on the constants values:

$$\gamma^{an}(G,\nu) \cong \frac{G}{4}\frac{1}{1-\nu}\frac{\pi}{\sqrt{2}}\left[\frac{2R_i}{\pi(R_e+R_i)-3(R_e-R_i)}\right]$$
$$\beta^{an}(G,\nu) \cong -\frac{G}{4}\frac{\pi}{1-\nu}\left[\frac{2R_i}{\pi(R_e+R_i)-3(R_e-R_i)}\right] \quad \text{(A- 33)}$$
$$d \cong \frac{\varepsilon_3^{an}}{4(1-\nu)}\left[1-\frac{6R_i}{\pi(R_e+R_i)-3(R_e-R_i)}\right]\frac{R_e^4 R_i}{(R_e+R_i)}$$
$$B \cong \frac{\varepsilon_3^{an}2G\pi}{128\sin\left(\frac{\pi}{8}\right)}\left[1-\frac{6R_i}{\pi(R_e+R_i)-3(R_e-R_i)}\right]\left(1+\frac{R_i}{R_e}\right)R_e^3$$

Δu_r^{an} can be written :

$$\Delta u_r^{an}\left(R_e, \frac{\pi}{8}\right) = -k_{an}\varepsilon_3^{an}$$
$$k_{an} = E + F$$

$$E = \left[\frac{1-2\nu}{4(1-\nu)}R_e^3 + \frac{2\nu}{4(1-\nu)}\left(\frac{\pi R_i R_e^3}{\pi(R_e+R_i)-3(R_e-R_i)}\right)\right] = \frac{1}{4(1-\nu)}\left[1-2\nu\left(1-\frac{\pi R_i}{\pi(R_e+R_i)-3(R_e-R_i)}\right)\right]R_e^3 \quad \text{(A- 34)}$$

$$F = 2\frac{R_i^4 R_e}{R_i^2 - R_e^2}\ln\left(\frac{R_e}{R_i}\right) - \left[\frac{R_i}{4(1-\nu)(Re+R_i)}\left(1-\frac{6R_i}{\pi(R_e+R_i)-3(R_e-R_i)}\right)R_e^3\right]$$
$$+\left[\frac{\pi}{128(1-\nu)}\left(1+\frac{R_i}{R_e}\right)\left(\frac{1}{\tan\left(\frac{\pi}{8}\right)}\left(1-4\ln\left(\frac{R_e}{R_i}\right)\right) - (2-4\nu)\frac{\pi}{8}\right)\left(1-\frac{6R_i}{\pi(R_e+R_i)-3(R_e-R_i)}\right)R_e^3\right]$$